ADVANCING EARTH AND SPACE SCIENCES

JGR Solid Earth

RESEARCH ARTICLE
10.1029/2025JB032083

Key Points:

- Depth phase sP waves are identified in local and regional seismic records
- Earthquake location is conducted within a Bayesian inversion framework, and location uncertainty is assessed simultaneously
- A thick seismogenic zone northwest of the M_w 7.1 mainshock area is observed, which indicates the potential of M5.5+ earthquake

Supporting Information:

Supporting Information may be found in the online version of this article.

Correspondence to:

P. Tong,
tongping@ntu.edu.sg

Citation:

Li, T., Chen, J., Yang, X., & Tong, P. (2026). Leveraging local depth phases for improved hypocenter analysis and discovery of a thick seismogenic zone in Ridgecrest, California. *Journal of Geophysical Research: Solid Earth*, *131*, e2025JB032083. https://doi.org/10.1029/2025JB032083

Received 3 JUN 2025
Accepted 22 DEC 2025

Author Contributions:

Conceptualization: Ping Tong
Data curation: Tianjue Li
Formal analysis: Tianjue Li, Jing Chen, Xu Yang, Ping Tong
Funding acquisition: Xu Yang, Ping Tong
Investigation: Tianjue Li
Methodology: Tianjue Li, Jing Chen, Xu Yang, Ping Tong
Resources: Ping Tong
Software: Tianjue Li
Supervision: Ping Tong
Validation: Tianjue Li
Visualization: Tianjue Li
Writing – original draft: Tianjue Li

Leveraging Local Depth Phases for Improved Hypocenter Analysis and Discovery of a Thick Seismogenic Zone in Ridgecrest, California

Tianjue Li[1], Jing Chen[1], Xu Yang[2], and Ping Tong[1,3]

[1]Division of Mathematical Sciences, School of Physical and Mathematical Sciences, Nanyang Technological University, Singapore, Singapore, [2]Department of Mathematics, University of California, Santa Barbara, CA, USA, [3]Earth Observatory of Singapore, Nanyang Technological University, Singapore, Singapore

Abstract

Accurate earthquake location is of fundamental importance for understanding seismogenic processes, revealing the Earth's interior structure, and mitigating seismic hazard. However, precisely determining the depth of an earthquake is often challenging due to the severe trade-off between focal depth and origin time, especially in the absence of nearby seismic stations. To address this challenge, we have developed an integrative procedure for reliably and efficiently identifying the sP depth phase in local and regional seismic records. After picking the traveltimes of first-arriving P, S waves and sP depth phases, we sequentially refine earthquake hypocenter (longitude, latitude and depth) and origin time within a Bayesian inversion framework. The efficacy of the proposed depth phase identification procedure and earthquake location method is validated through the analysis of small-to-moderate aftershocks that occurred within 2 months of the 2019 M_w 7.1 Ridgecrest earthquake. Our study shows that including depth phases can significantly reduce location uncertainty in depth by a factor of five. Moreover, the results achieved by jointly using first arrivals and depth phases are less dependent on the background velocity model, enabling more accurate location estimates for 86.6% of the examined earthquakes. In regions northwest of the mainshock nucleation area, the base of the seismogenic zone is located generally below 10 km, likely sandwiching a much shallower brittle-to-ductile transition zone (<4 km) beneath the Coso geothermal site. This locally abrupt change in rock rheology may modulate the rupture propagation of large earthquakes.

Plain Language Summary

Accurate earthquake hypocenter (longitude, latitude, and depth) and origin time are of fundamental importance in geoscience studies. However, it is often difficult to precisely constrain the earthquake depth due to the trade-off between focal depth and origin time. To overcome this challenge, we have developed a systematic procedure for identifying the sP depth phase in local and regional seismic records. Such source-side surface reflections (e.g., sP) are very sensitive to the earthquake depth, and by jointly using the depth phase as well as first-arriving P and S waves, we can precisely constrain both earthquake hypocenter and origin time. Because the earthquake location is conducted within a Bayesian inversion framework, it is natural to assess the location uncertainty. Using the new phase identification procedure and earthquake location method, we have located 277 aftershocks with magnitude from 2.0 to 5.0 of the 2019 M_w 7.1 Ridgecrest earthquake more accurately. Except for the Coso geothermal site, we find a thick seismogenic zone in regions northwest of the mainshock nucleation area, which is 0.6–9.8 km deeper than previous estimates, indicating a potential risk for future earthquakes with magnitude larger than 5.5.

1. Introduction

Accurate determination of earthquake hypocenters is vital for identifying the seismicity pattern within a region and delineating the fault geometry at depth (e.g., Ross et al., 2019). It serves as the basis for understanding the seismogenic processes (e.g., Hauksson & Meier, 2019) and is instrumental in assessing future earthquake risk potential (e.g., earthquake shaking potential for California, Branum et al., 2008). Reliably determining earthquake hypocenters is also a prerequisite for various other studies, including obtaining point-source focal mechanisms (e.g., Zhu & Helmberger, 1996), inferring kinematic finite-fault rupture processes (e.g., Ji et al., 2003), conducting passive-source seismic tomographic inversion (e.g.., Rawlinson et al., 2010), as well as discriminating underground explosions from natural earthquakes (e.g., Bowers & Selby, 2009; Koper et al., 2024). There are various earthquake location refinement packages available, such as HypoDD (Waldhauser & Ellsworth, 2000), Growclust (Trugman & Shearer, 2017), and NonLinLoc (Lomax et al., 2000). Each package has its pros and cons when

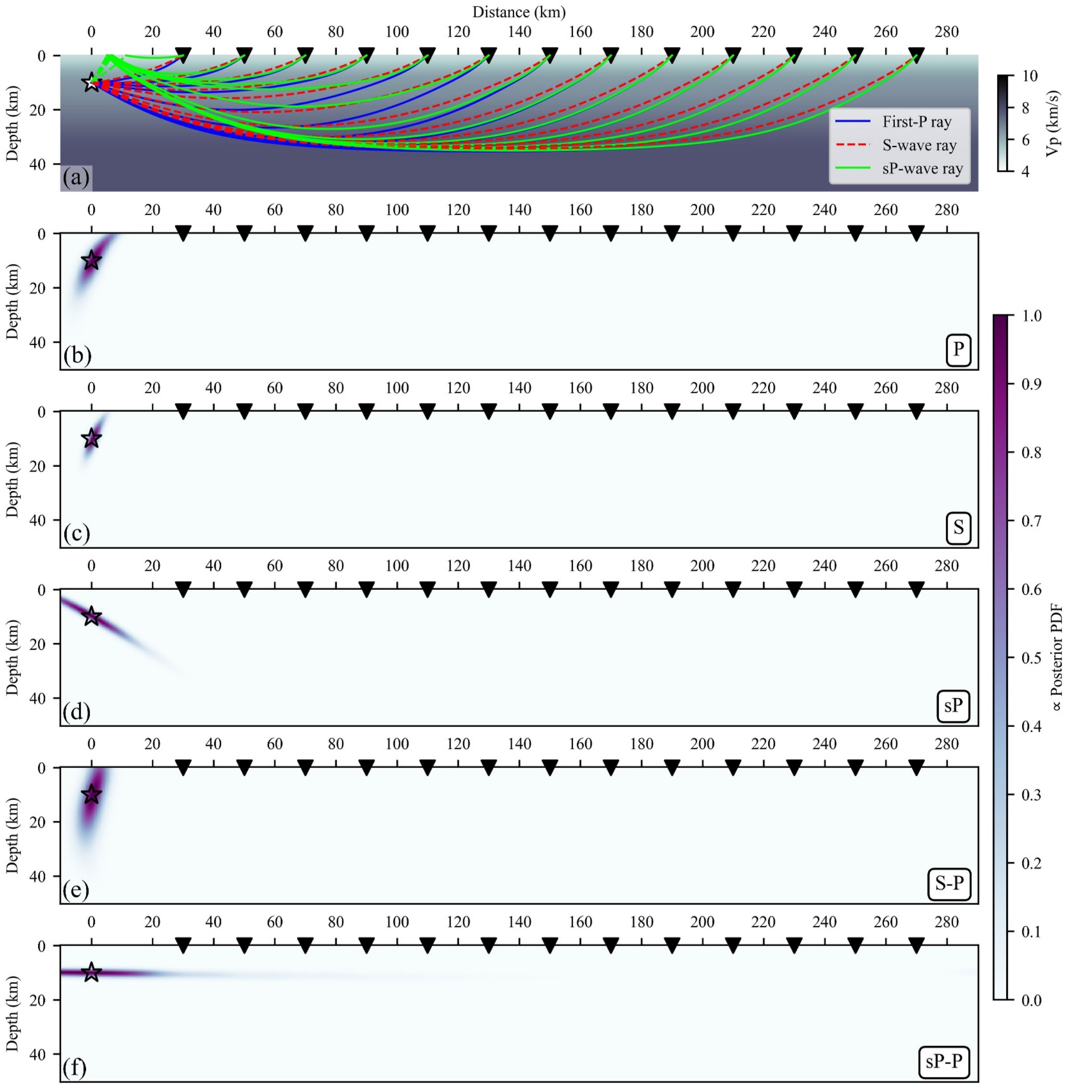

Figure 1. Phase traveltime sensitivity in locating the spatial coordinates of an earthquake. (a) Phase ray path in a 1D smoothed model. The white star with black edge denotes the earthquake, and the black inverted triangles represent the seismic stations. The solid blue curve denotes the P-wave ray, the dashed red curve denotes the S-wave ray, and the dashed/solid lime curve shows the upward S-leg/P-leg of the sP-wave ray. (b) The color-coded region with probability density function (PDF) is equivalent to the stacked equal traveltime (ET) surface of P waves from multiple observations, which is used as the quantitative measure to represent the phase traveltime sensitivity to the quake source. Note seismic stations are only installed on one side of the earthquake. (c, d) The same as (b) but for S and sP phases. (e) The color-coded region with PDF is the stacked S-P equal differential arrival time (EDT) surface from multiple observations. (f) The same as (e) but for the sP-P EDT surface. Here, following Zhou (1994), the ET/EDT surface from one observation can be defined as the collection of spatial points where the predicted phase arrivals/phase arrival differences approximate the observations within the tolerable uncertainty, thus any point on the ET/EDT surface could be the event hypocenter.

locating earthquakes and revealing seismicity patterns according to a recent synthetic controlled experiment (Yu et al., 2025). However, challenges persist in accurately estimating earthquake location uncertainty, along with often large ambiguities in determining the focal depth (Figure 1).

Uncertainty in earthquake location stems from two main sources: random errors associated with phase picking and systematic errors introduced by either overly simplified velocity models or uneven seismic station coverage. In regions with well-defined three-dimensional (3D) velocity models, such as Southern California, realistic models are routinely adopted to mitigate systematic errors (e.g., Hauksson et al., 2012). In areas lacking accurate 3D velocity models, correction strategies like static station terms and source-specific station terms (e.g., Richards-

Dinger & Shearer, 2000) are employed to reduce biases. Typically, the background velocity model is assumed to be known and fixed during the earthquake location processes (Lomax et al., 2009). Uneven seismic station coverage usually results in elongated error ellipses for earthquake epicenters (Lomax et al., 2009), while this bias can be alleviated to some extent by adopting geographic weighting schemes (e.g., Ruan et al., 2019). Random picking errors contribute to location uncertainty by acting as weighting factors in forming the objective function (Lomax et al., 2009). However, determining picking errors in a relatively objective way is still under exploration (e.g., Armstrong et al., 2023; Peterson et al., 2021).

The large uncertainty in determining earthquake depth arises from the incomplete observations. Because in most cases we do not have instrument directly below the source, there is trade-off between earthquake origin time and focal depth when interpreting the first arrivals. Such challenge becomes more pronounced when only distant seismic stations are available (e.g., Figure S1 in Supporting Information S1; stations located more than 1.4 times of the earthquake depth, Gomberg et al., 1990). Although designing the objective function in terms of differential arrival times can eliminate the earthquake origin time from the inversion process (e.g., Tong et al., 2024; Zhou, 1994), the commonly used first-arriving P and S waves are typically picked at stations several times farther from the earthquake epicenter than the focal depth, providing limited constraint on the depth (Figure S2 in Supporting Information S1). To deal with this challenge, one approach is to deploy temporary seismic stations directly above the source region following a large earthquake (e.g., Cochran et al., 2020; White et al., 2021). However, this solution is expensive and feasible only in limited regions. Another strategy is to use depth-sensitive signals in seismic records, such as the amplitude spectra of short-to-intermediate period surface waves or depth phases such as pP and sP waves, which undergo surface reflection or mode conversion usually on the source side (e.g., Stein & Wiens, 1986; Tsai & Aki, 1970). Over the past few decades, significant efforts have been made to utilize depth phases for refining earthquake locations (e.g., Craig, 2019; He et al., 2019; Ma, 2010; Umino et al., 1995; Yu et al., 2019; Yuan et al., 2020). Currently, the routine identification of depth phases in teleseismic records has become feasible for refining earthquake locations, as seen in global catalogs like ISC-EHB catalog (usually for magnitudes larger than 4.5, Weston et al., 2018) and NEIC catalog (with magnitude larger than 5.5, Yeck et al., 2025). At local and regional distances, depth phase identification primarily relies on waveform modeling for earthquakes with magnitude greater than 2.5, where the associated focal mechanism is either estimated simultaneously or predetermined (e.g., He et al., 2019; Ma, 2010; Yu et al., 2019). Notably, Yuan et al. (2020) proposed a depth-scanning algorithm that employs phase-shifted first-P wavelets as templates to match likely depth-related seismic phases within a local 1D velocity model. Though the depth-scanning algorithm is typically efficient and provides accurate depth estimates, it may encounter challenges or introduce biases when strong horizontal heterogeneities exist in the actual velocity model.

In this study, we developed a systematic approach that leverages the distinctive sensitivities of the first-arriving P, S and depth phases to accurately and precisely locate earthquakes. Without the need for a predetermined focal mechanism, we first introduce a method that combines the advantages of polarization filtering (e.g., Vidale, 1986) and signal deconvolution (e.g., Woodgold, 1999) to reliably and efficiently identify sP depth phases in local and regional seismic records, which are prominent due to the mode conversion at the free surface (e.g., Aki & Richards, 2002). Then, the earthquake hypocenter and origin time are sequentially constrained by jointly using first arrivals and depth phases within a Bayesian framework. Structural heterogeneities are accounted for by obtaining phase traveltimes through solving the eikonal equation within a realistic 3D background velocity model. We validate the novel approach for depth phase identification and the earthquake location scheme in the Ridgecrest area of California. Using the characterization of the seismogenic zone as an example, we emphasize that accurately determining earthquake depths is crucial for understanding the local seismogenic processes.

2. Data

In the Ridgecrest region of California, we analyze three-component waveforms of 697 aftershocks that occurred between 1 August and 30 September 2019, following the M_w 7.1 mainshock on July 6th (Figure S3 in Supporting Information S1). Aftershocks with magnitudes greater than 2.0 are chosen from the standard Southern California Seismic Network (SCSN) catalog (Hutton et al., 2010). Event waveforms are downloaded from the Caltech/USGS Southern California Seismic Network (SCSN; doi: 10.7914/SN/CI) and its collaborative partner networks including 7Q (doi: 10.7914/SN/7Q_2019), GS (doi: 10.7914/SN/GS), NN (doi: 10.7914/SN/NN), and PB (Plate Boundary Observatory Borehole Seismic Network), stored at the Southern California Earthquake Data Center

(SCEDC, 2013). Additionally, we obtain phase arrival times from the SCEDC (2013) and use these expert-reviewed P and S arrivals for later signal processing.

3. Method

3.1. Preparing Arrival Times of First-Arriving P and S Waves

To obtain first-arriving P and S wave arrival times in a consistent way and expand the data volume as much as possible, we use the Akaike Information Criterion (AIC, e.g., Fang et al., 2022) to determine phase onsets and assess the associated picking uncertainties. First, we select high-quality waveforms. For records lacking labeled phase arrivals from the SCEDC, we calculate the theoretical first-arriving P and S arrival times at each seismic station using the SCSN catalog location and the standard 1D velocity model for Southern California (Hadley & Kanamori, 1977; hereafter referred to as the HK model). Based on these expert-reviewed or theoretically calculated phase arrival times, we compute the P-wave signal-to-noise ratio on each vertical component. The noise level is estimated from 2.0 to 0.5 s before the first-P arrival, while the signal is assessed from 0.5 s before to 1.0 s after the first-P arrival. Event waveforms with a P-wave SNR greater than 5.0 are selected and retained.

Next, we employ the AIC phase picker to enhance the precision of the P-wave phase onset on each vertical component for the selected high-quality waveforms. The picking process is conducted automatically within a fixed time window from 1 s before to 1 s after the referenced P-wave onset which is either from the data center or theoretical calculation. When the automated phase picker fails to accurately identify the phase onset, manual tuning of the time window is performed. Then, we assess the phase picking uncertainty in a similar way as the practice of Peterson et al. (2021). In detail, the automated phase picking process is repeated multiple times (default 200 times) in a series of time windows to assess the phase picking uncertainty. Centered on the refined first-P arrival time t_P, the time window is defined as $[t_P - \Delta t, t_P + \Delta t]$, where Δt (in seconds) follows a uniform distribution, $\Delta t \sim U(0.25, 0.75)$. The mean of these 200 phase picks is used to update the first P-wave onset, and the associated standard deviation is employed to estimate the associated picking error (Figure S4a in Supporting Information S1). For waveforms with updated P-wave onset times, we refine the S-wave arrival times using the same procedure, but applied to the combined horizontal component following the practices of Fang et al. (2022), that is, $\sqrt{E^2 + N^2}$, where E and N refer to the east and north channels, respectively (Figure S3b in Supporting Information S1). After discarding outlier phase picks (i.e., those beyond five standard deviations) and closely spaced P and S arrivals (i.e., $t_s - t_P < 0.5$ s), we retain a total of 6,085 first-arriving P-wave picks and 6,072 first-arriving S-wave picks from 320 aftershocks, an average increase of 48% compared to those available at SCEDC (Text S1 and Figure S5 in Supporting Information S1).

3.2. Preparing the Database of sP Depth Phase

Previous studies have summarized several diagnostic characteristics for identifying sP waves at local and regional distances (e.g., Ma, 2010; Umino et al., 1995):

1. sP waves are typically observed on vertical component seismograms;
2. sP waves approach seismic stations in a similar direction as that of direct P waves;
3. sP waves propagate with an apparent velocity slower than direct P waves but faster than direct S waves;
4. sP waves have a predominant period slightly longer than that of direct P waves and comparable to that of direct S waves;
5. The amplitudes of sP waves are about 50%–200% of those of the direct P waves;
6. The arrival time lag between sP and first-arriving P waves from the same earthquake (e.g., phase pairs of sPg-Pg and sPn-Pn) is nearly constant across seismic stations.

Based on these characteristics, we have designed five quantitative metrics for the reliable phase identification of sP waves:

1. The dominant energy of an sP wave is expected to be concentrated in the vertical–radial (Z-R) plane. Thus, the sP-wave amplitude in the Z-R plane (A_{sP}^{Z-R}) should be larger than its amplitude on the tangential component (T), that is, $A_{\mathrm{sP}}^{Z-R}/A_{\mathrm{sP}}^{T} > 1.0$;

2. sP waves must be sufficiently strong to stand out from the background noise. So, on the vertical component, we require that the amplitude A_{sP}^{Z} of every potential sP wave is at least half of that of the corresponding first-P wave, that is, $A_{\mathrm{sP}}^{Z}/A_{\mathrm{P}}^{Z} > 0.5$;
3. sP waves are expected to have polarization similar to the first-P waves, with a comparable incidence angle (θ) in the Z-R plane, that is, $\left|\theta_{\mathrm{sP}}^{Z-R} - \theta_{\mathrm{P}}^{Z-R}\right| < 20°$;
4. sP and first P waves should exhibit an identical degree of polarization (DOP) in the Z-R plane, specifically, $\left|\mathrm{DOP}_{\mathrm{sP}}^{Z-R} - \mathrm{DOP}_{\mathrm{P}}^{Z-R}\right| < 0.1$. Note that the DOP is defined as $\mathrm{DOP}^{Z-R} = (\lambda_1 - \lambda_2)^2/(\lambda_1 + \lambda_2)^2$, where $\lambda_i (i = 1, 2)$ represents the eigenvalues $(\lambda_1 \geq \lambda_2)$ of the principal components of the particle motion, as proposed by Samson and Olson (1980);
5. sP waves are expected to have a dominant frequency $f^{Z,\mathrm{peak}}$ comparable to that of the first P waves on the vertical component, that is, $\left|f_{\mathrm{sP}}^{Z,\mathrm{peak}} - f_{\mathrm{P}}^{Z,\mathrm{peak}}\right| < 2.0$ Hz.

These quantitative metrics are applied to highlight likely depth phase signals while muting others through a time-domain polarization filter. Note that the designed metrics 1) and 4) represent the same property that energy in the sP phase is expected to be polarized into the Z-R plane but from two different aspects. The aim of including such reductant metrics is to mutually validate the sP wave property in a noisy real world. Metric 3) applies for distant records where the epicentral distance is larger than the event focal depth. We conduct the filtering process in this way: Given a velocity model and a predetermined epicenter, all candidate depth phase signals for a single event are then transformed to the depth domain and stacked. The resulting stacked depth profile reveals the most probable focal depth. This preferred focal depth, together with the fixed epicenter, is used to predict the arrival of the sP depth phase at each station within the velocity model. Phase picking and uncertainty estimation are subsequently performed using the same procedure applied to the first-arriving P and S waves. The complete process for depth phase identification, phase picking, and data quality control in constructing the sP database is summarized in Figure 2. Two synthetic experiments with fixed observational azimuth or epicenter distance are presented in the supplementary material (Figures S6 and S7 in Supporting Information S1) to provide an overview of the effectiveness of the designed algorithm in identifying depth phases in local seismic records. We now turn to the technical details of applying the algorithm to real seismic data.

3.2.1. Time-Domain Polarization Filtering for sP Depth Phase Detection

To develop an efficient approach for depth phase identification, we first design a time-domain polarization filter to simplify waveforms based on the aforementioned five quantitative metrics. This filter has similar features as classical polarization filters (e.g., Sollberger et al., 2023; Vidale, 1986) but incorporates a broader range of attributes to more accurately isolate target signals. Specifically, we treat every sampling point on the waveform as the onset of a potential sP phase and compute the instantaneous $A_{\mathrm{sP}}^{Z-R}/A_{sP}^{T}$ ratio within a sliding time window $[t_i - 0.05, t_i + 0.45]$. Here, t_i (in seconds) refers to the phase onset of the i-th potential sP wave, and the window shifts forward by two sampling points (0.02 s) each time to balance the computational cost and the accuracy of phase onset identification (the red curve in Figure 3b). To ensure continuous amplitude measurements along the time axis, we integrate the windowed absolute signal and treat it as the phase amplitude. For instance, in the Z-R plane, we define the amplitude of a potential sP wave as

$$A_{sP}^{Z-R} = \int_{t_i-0.05}^{t_i+0.45} \sqrt{Z(t)^2 + R(t)^2}\,dt, \tag{1}$$

where $Z(t)$ and $R(t)$ represent the vertical and radial components, respectively. In the tangential direction, we define the amplitude of a potential sP wave as

$$A_{sP}^{T} = \int_{t_i-0.05}^{t_i+0.45} |T(t)|\,dt, \tag{2}$$

where $T(t)$ represents the tangential-component waveform. Within the same time window, we also compute four other instantaneous attributes of the potential sP wave, including the $A_{\mathrm{sP}}^{Z}/A_{\mathrm{P}}^{Z}$ ratio (the blue curve in Figure 3b) and $f_{sP}^{Z,\mathrm{peak}}$ (Figure 3d) which are measured in a similar integral manner. The signal polarization attributes, such as $\theta_{\mathrm{sP}}^{Z-R}$ (the red curve in Figure 3c) and $\mathrm{DOP}_{\mathrm{sP}}^{Z-R}$ (the blue curve in Figure 3c), are directly measured in the Z-R

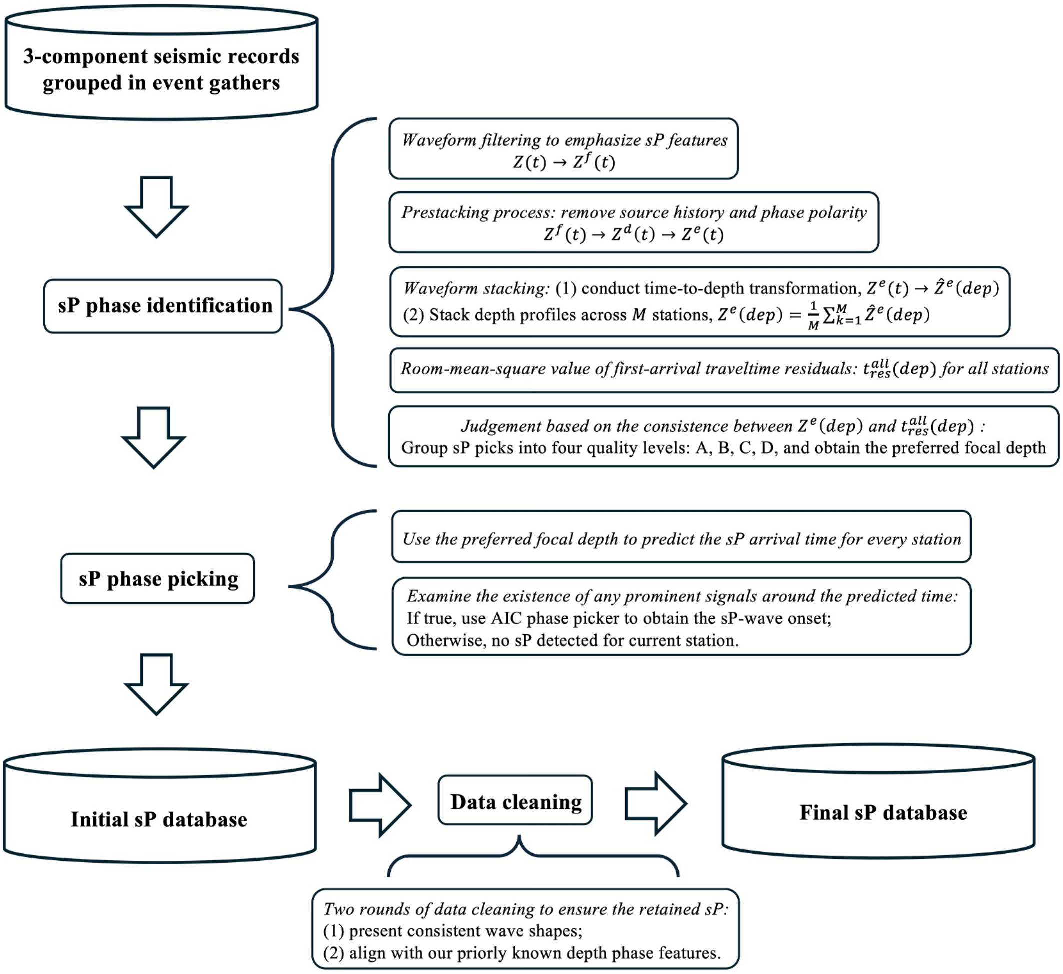

Figure 2. Flowchart of preparing the depth phase sP waves.

plane. Once all these instantaneous attributes are computed, the vertical-component waveform within the time window $[t_i - 0.05, t_i + 0.45]$ is either retained if all the five quantitative metrics meet the predefined criteria (e.g., above or near the dashed lines in Figures 3b–3d) or muted to zero otherwise. Additionally, portions outside the time window $[t_i - 0.05, t_i + 0.45]$ are muted to zero. The resultant waveform is denoted as $Z_i(t)$. Repeating this procedure for every time window, a filtered signal is obtained ($Z^f(t)$ in Figure 3e) by averaging all the windowed waveforms

$$Z^f(t) = \frac{1}{N}\sum_{i=1}^{N} Z_i(t), \tag{3}$$

where N represents the total number of time windows considered. This filtering process greatly simplifies the original waveforms, facilitating subsequent depth phase identification. To further enhance waveforms stacking across different stations in subsequent analyses, we deconvolve the first-P wave (captured 0.05 s before and 0.45 s after the phase onset) from the filtered signals to increase the SNR of target phase arrivals, following the procedure described by Crag (2019). The resulting signal ($Z^d(t)$ in Figure 3e) is then transformed to its associated envelope ($Z^e(t)$ in Figure 4b) for removing variations in phase polarity.

3.2.2. Stacking Candidate sP Phases in the Depth Domain

After aligning $Z^e(t)$ to the onset of the first-P arrival, each subsequent time sample represents a potential sP-P differential arrival time. For each differential arrival time, along with a background velocity model and an

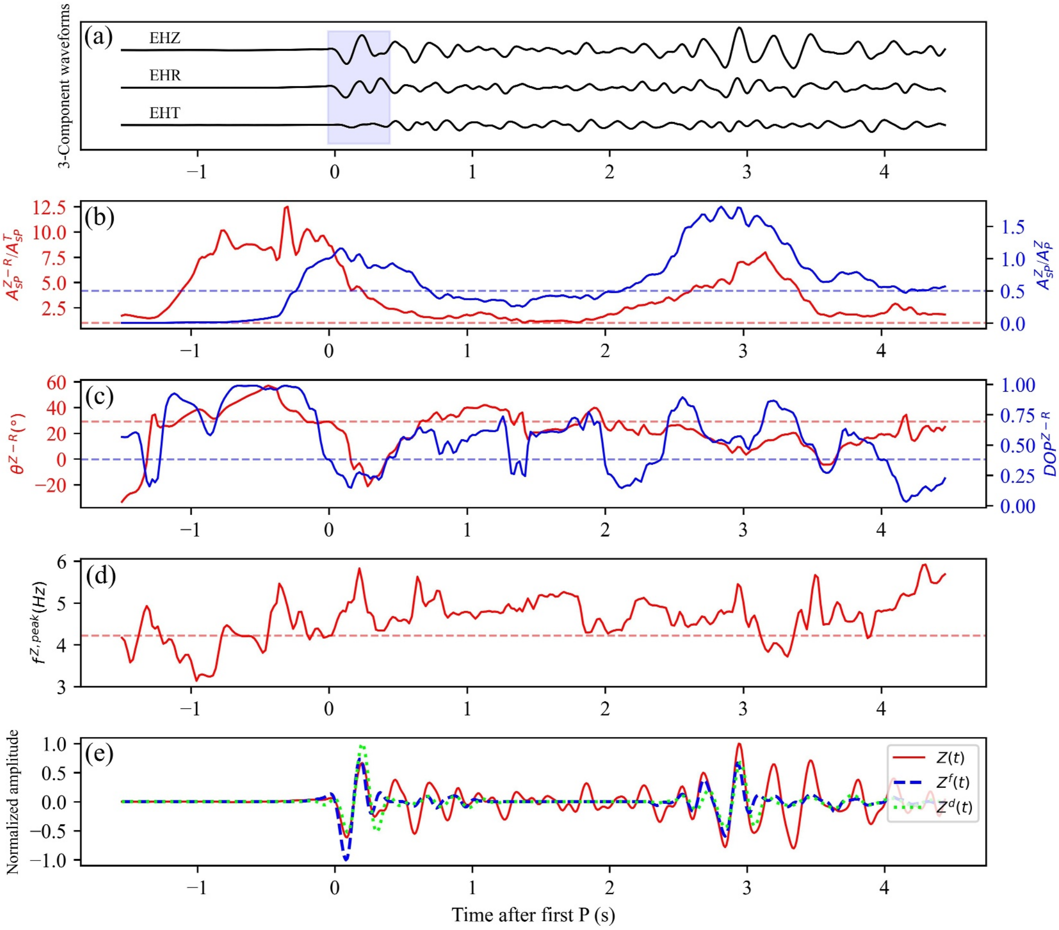

Figure 3. An example of using the multiple instantaneous attributes to filter the raw event waveform. (a) The 3-component event waveforms were recorded at station PB.B916 from an earthquake of M2.8 occurring on 2019-09-29T12:08:19.570Z. The earthquake situates at a depth of 8.95 km, and the source-receiver distance is 58.9 km. The waveform segment under the blue band denotes the windowed first-P wave. (b) The instantaneous amplitude ratio of the potential sP waves in the Z-R plane over itself on the tangential component (red curve), and the instantaneous amplitude ratio of the sP waves over the first P on the vertical component (blue curve). The dashed lines denote the threshold used to filter the raw waveform. (c) The instantaneous incidence angle of the potential sP waves in the Z-R plane (red curve) where the positive values mean the particle moves along the radial direction, whereas the negative values mean the particle moves against the radial direction. The instantaneous degree of polarization of the potential sP waves in the Z-R plane is shown as blue curve. The dashed lines denote the instantaneous polarization attributes of the first-P wave. (d) The instantaneous peak frequency of the potential sP waves on the vertical component. The dashed line denotes the instantaneous peak frequency of the first-P wave. (e) The original event waveform $Z(t)$ shown as red curve is compared to its filtered signal $Z^f(t)$ (dashed blue curve), and to the deconvolved signal $Z^d(t)$ (dotted lime curve).

event epicenter (e.g., the catalog epicenter), we can estimate the corresponding focal depth. In this study, we choose the 3D community velocity model CVM-S4.26 (Lee et al., 2014) as the background velocity model. To minimize potential biases introduced by catalog locations, we have updated all event epicenters using the newly picked first-P arrival times and S-P differential arrival times in the CVM-S4.26 model. Assuming a discrete set of possible focal depths $\{\mathrm{dep}_j\}$ within a range from the free surface to slightly beyond the typical maximum seismogenic depth (approximately 20 km for the Ridgecrest region, California; Nazareth & Hauksson, 2004), we predict the associated sP-P differential arrival times $\{t_{\mathrm{sP-P}}^{j}\}$. Here the first-P arrival times are calculated by numerically solving the eikonal equation using the fast-marching method, while the sP-wave arrival times are obtained by solving the eikonal equation twice using a multi-stage fast-marching method (Rawlinson & Sambridge, 2005; White et al., 2020). Since the sP-P differential arrival time generally monotonically increases with focal depth, the transformation of the filtered envelope waveform $Z^e(t)$ from the sP-P time domain to the 1D focal

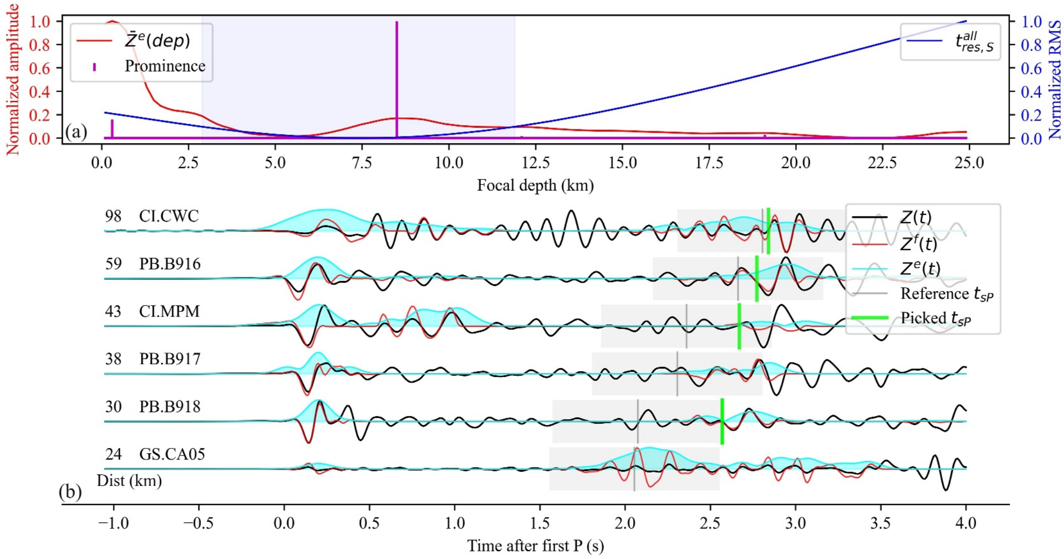

Figure 4. An example of depth phase identification. The event waveforms are from an earthquake of M2.8 occurred on 2019-09-29T12:08:19.570Z, and the earthquake is at 8.95 km depth according to the Southern California Seismic Network catalog. (a) The solid red curve denotes the stacked sP wave $\overline{Z}^e(\text{dep})$ in focal depth domain, and the purple stem plot shows its corresponding peaks. The solid blue curve shows the root mean square values of traveltime residuals versus focal depth for all available S waves. When there is one dominant peak in $\overline{Z}^e(\text{dep})$ within the depth range at which the traveltime residuals do not differ by more than 10% from its trough (blue shading zone), and the peak height in $\overline{Z}^e(\text{dep})$ is the global maximum, we label the sP waves for this event as quality A and regard that peak position as the preferred focal depth. (b) The black, red and cyan curves represent the original event waveform $Z(t)$ (vertical component), filtered waveform $Z^f(t)$, and deconvolved signal envelope $Z^e(t)$, respectively. Note the signals have been normalized and aligned to the first P onset. At the beginning of each signal, we also present the source-receiver distance (dist) and station name. The vertical gray bar indicates the referenced sP onset, which is calculated using the preferred focal depth determined in (a). Within 0.5 s from the referenced sP onset (the gray-shading zone), we pick the final used sP onset as denoted by the vertical lime bar. For station PB.B917, no good sP wave is retained after data cleaning.

depth domain can be easily established to obtain $\hat{Z}^e(\text{dep})$. We conduct this transformation at each station. For a given event, the resulting signals across all stations $\{\hat{Z}^e_k(\text{dep})\}$ are averaged to obtain a stacked depth profile:

$$\overline{Z}^e(\text{dep}) = \frac{1}{M}\sum_{k=1}^{M} \hat{Z}^e_k(\text{dep}), \tag{4}$$

where M is the total number of seismic stations used (the red curve shown in Figure 4a).

To more effectively highlight the depths at which the transformed signals are constructively stacked, we compute the peaks of $\overline{Z}^e(\text{dep})$ (the purple stem plot in Figure 4a). The height of each peak is defined using topographic prominence, a measure commonly used in mountaineering to describe the height of a peak relative to its surroundings (e.g., Kirmse & de Ferranti, 2017). To further enhance the confidence in depth phase identification, we also calculate the root-mean-square (root mean square (RMS)) of the residuals between the picked and predicted traveltimes of P waves, S waves, and S-P differential arrival times, as a function of focal depth (Figure 4a, Figures S8a and S9a in Supporting Information S1). For example, we compute the RMS of first-arriving S-wave tracveltime residuals across all available stations ($t^{\text{all}}_{\text{res}}(\text{dep})$, the solid blue curve in Figure 4a) using the CVM-S4.26 model. The event epicenter used in these calculations is the same as that used for the time-to-depth transformation. By examining whether and how the peaks in $\overline{Z}^e(\text{dep})$ coincide with the troughs in the $t^{\text{all}}_{\text{res}}(\text{dep})$ curve, we determine the most likely focal depth of the event. In particular, we first find the trough of the $t^{\text{all}}_{\text{res}}(\text{dep})$ curve, with

$$\text{dep}^* := \underset{\text{dep}}{\text{argmin}}\, t^{\text{all}}_{\text{res}}(\text{dep}), \tag{5}$$

Then, we define a focal depth interval $\left[\mathrm{dep}_1, \mathrm{dep}_2\right]$ that likely encloses the true focal depth,

$$\mathrm{dep}_{1,2} \coloneqq \underset{\mathrm{dep}}{\operatorname{argmin}}\left(\left|t^{\mathrm{all}}_{\mathrm{res}}(\mathrm{dep}) - 1.1 \cdot t^{\mathrm{all}}_{\mathrm{res}}(\mathrm{dep}^*)\right|\right), \tag{6}$$

We identify the largest peak in $\overline{Z}^e(\mathrm{dep})$ within $\left[\mathrm{dep}_1, \mathrm{dep}_2\right]$, and assigns its location as the preferred focal depth for the event. In practice, according to how many peaks in $\overline{Z}^e(\mathrm{dep})$ exist within $\left[\mathrm{dep}_1, \mathrm{dep}_2\right]$ and whether the largest peak in this segment is the global maximum, we group the sP waves associated with the examined event into different quality levels (see more details in Text S2 and Figures S8–S13 of Supporting Information S1). To assess the influence of individual stations on the stacked depth profile, we performed jackknife tests (Text S2 and Figure S14 in Supporting Information S1). The results indicate that all station records contribute to the preferred depth estimate, although none is indispensable.

3.2.3. sP Phase Picking and Uncertainty Estimation

Once the preferred focal depth is determined, we use it to predict the sP arrival time (t^*_{sP}) at each station in the CVM-S4.26 model. We then inspect each vertical-component waveform $Z(t)$ for prominent signals around the predicted phase arrival. A signal is considered prominent if, within the time window $[t^*_{\mathrm{sP}} - 0.5, t^*_{\mathrm{sP}} + 0.5]$, its maximum absolute amplitude is at least half that of the first P-wave and at least 1.5 times as large as the average amplitude within the same window, computed as $\int_{t^*_{\mathrm{sP}}-0.5}^{t^*_{\mathrm{sP}}+0.5} |Z(t)|dt$. If such a prominent signal is detected, we use the AIC phase picker, as used previously for detecting first-arriving P and S phases, to determine the sP onset and estimate its picking error. The only difference is the choice of time window: the picker is applied once within $[t^*_{\mathrm{sP}} - 0.5, t^*_{\mathrm{sP}} + 0.5]$ to refine the sP arrival time t_{sP}. However, if the phase picker fails to accurately pick the sP onset, manual tuning of the time window is allowed. For assessing the uncertainty of phase picking, the time window is set as $[t_{\mathrm{sP}} - \Delta t, t_{\mathrm{sP}} + \Delta t]$, where Δt (in seconds) follows a uniform distribution, $\Delta t \sim U(0.02, 0.12)$ by default. Examples of the picked phase data and the associated waveform for a chosen event is shown in Figure 5.

3.2.4. Construction and Quality Control of the sP-Wave Database

In total, 1,107 depth phases have been identified from the seismic records of the examined events. To construct a high-quality sP database, we perform two rounds of data cleaning to ensure the picked sP arrivals exhibit consistent waveforms and typical depth-phase characteristics (see details of how we conduct the data cleaning in Text S3, Figures S15 and S16 of Supporting Information S1). In the first step, 47 sP picks do not pass the consistent waveform test thus are removed from our sP database. At the second filtering stage, we further remove an additional 238 sP picks after checking the five sP phase metrics. Following the two rounds of data cleaning, we retain 822 high-quality sP arrivals from 277 aftershocks in the Ridgecrest region, California, accounting for 86.6% of the analyzed events (Figure S3 in Supporting Information S1). On average, there are 3 sP-wave picks per earthquake (Figure 6). The retained sP waves exhibit high consistency in shape (Figure S16d in Supporting Information S1), and the accuracy of phase picking is high, as evidenced by the close agreement between sP-P differential arrival times obtained from the AIC phase picker and those measured from phase envelope peaks (Figures S17a and S17b in Supporting Information S1). In the following section, we focus on these 277 aftershocks to relocate their hypocenters and origin times using both first arrivals and sP depth phases.

3.3. Bayesian Inversion for Locating Earthquakes

Given the well-known trade-off between earthquake origin time and focal depth (Gomberg et al., 1990), we address this challenge by adopting a three-step inversion strategy within a Bayesian framework to determine the four-dimensional earthquake location (longitude, latitude, depth, origin). Here, we briefly introduce the procedures for each stage; detailed techniques are provided in Appendix A. In the first step, we utilize the first-P arrival times, which typically have better azimuthal coverage than other observations (e.g., first-arriving S or later phases), to infer the earthquake hypocenter (mainly the epicenter). During this step, the origin time is fixed to the standard catalog value, and each P-wave arrival time is weighted according to its picking uncertainty. At the same time, we reduce the influence of uneven station distribution via a geometrical correction following Ruan et al. (2019). In the second step, we modify the earthquake hypocenter posterior to be homogeneous along the depth direction (Figures 7a–7c) and use it as the prior distribution. Then, we update the earthquake hypocenter by using both S-P

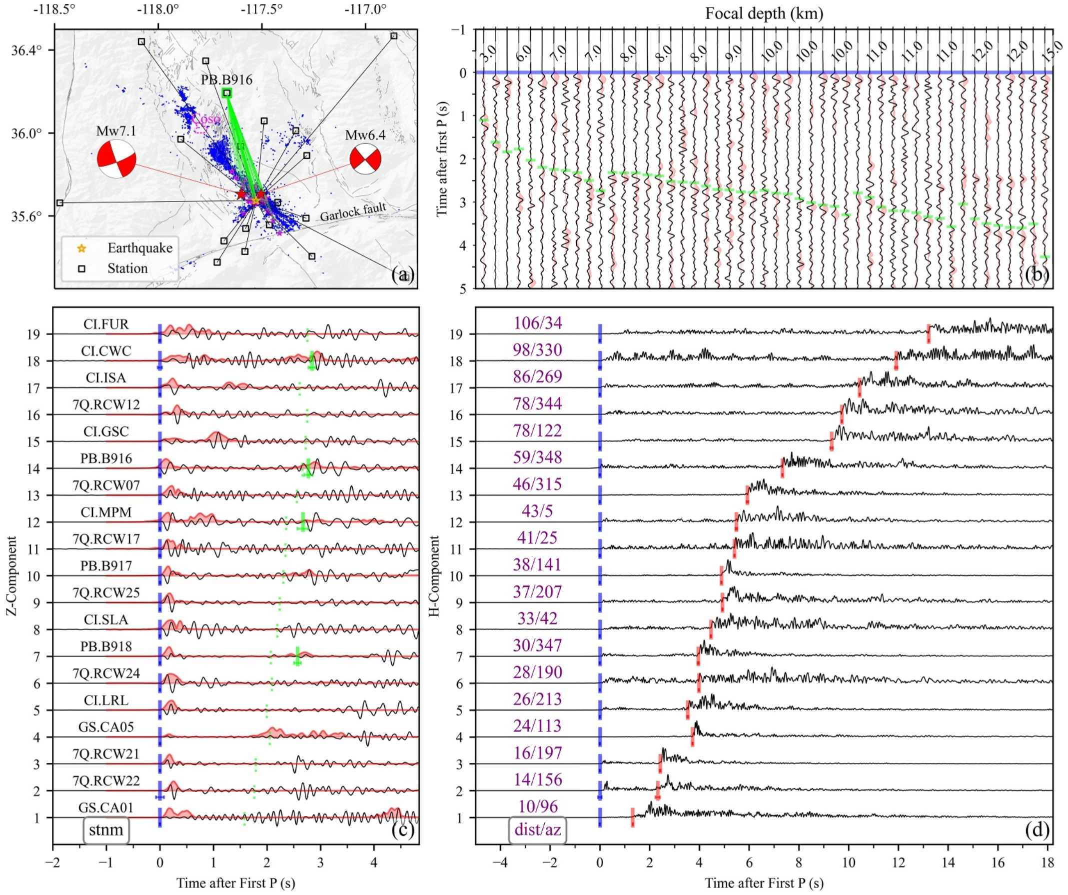

Figure 5. An example of the picked phase data and the associated waveforms. (a) Map view of event and station distribution. Blue dots show the background seismicity with magnitude larger than 2.0 from the Southern California Seismic Network (SCSN) catalog between 5 June and 30 September 2019. We present the picked sP waves from a group of earthquakes (magenta open stars) in (b) that are recorded by station PB.B916 (lime open square) within the azimuth range between 343 and 357°. Besides, we also display the picked P and S waves from a M2.8 earthquake which occurred on 2019-09-29T12:08:19.570Z with its epicenter denoted by the orange open star. Recording stations are represented by black open squares. Magenta dashed line outlines the Coso geothermal field following Monastero et al. (2005). Two filled red stars represent the foreshock and mainshock of the Ridgecrest earthquake sequence, with the focal mechanism from the SCSN focal mechanism catalog. (b) The present vertical-component velocity waveforms have been bandpass filtered between 1 and 8 Hz. We align waveforms to first P (blue line) and sort them according to the updated focal depth. The picked sP waves are marked by the lime bars, and the red-filled curves show the deconvolved signal envelopes ($Z^e(t)$), where a larger amplitude of $Z^e(t)$ suggests a higher likelihood of the existence of sP waves. (c) The picked first-P (blue bars) and sP (lime bars) waves from a M2.8 earthquake are marked on the vertical-component waveforms. Both the picked phase onset (vertical bar) and the associated one-standard-deviation interval of picking uncertainty (horizontal bar) are displayed. The recording seismic stations (stnm) are denoted above each waveform. (d) The picked S waves (red bars) from the M2.8 earthquake are marked on the horizontal-component ($\sqrt{E^2 + N^2}$) waveforms. The recording epicentral distance (dist) and azimuth (az) are present above each waveform.

and sP-P differential arrival times. Importantly, the inferred earthquake location is independent of the origin time (Figures 7d–7i) due to the use of differential arrival times. The involvement of sP waves further reduces the location uncertainty along the depth direction (Figures 7f–7i). In the third and final step, we use the maximum likelihood hypocenter to predict the first-P traveltimes and refine the origin time by fitting the observed first-P arrivals (Figure 7j).

4. Results

Through the analysis of two months of aftershock records of the M_w 7.1 mainshock on 6 July 2019, in the Ridgecrest region, California, we have successfully identified 822 sP-wave picks from 277 earthquakes

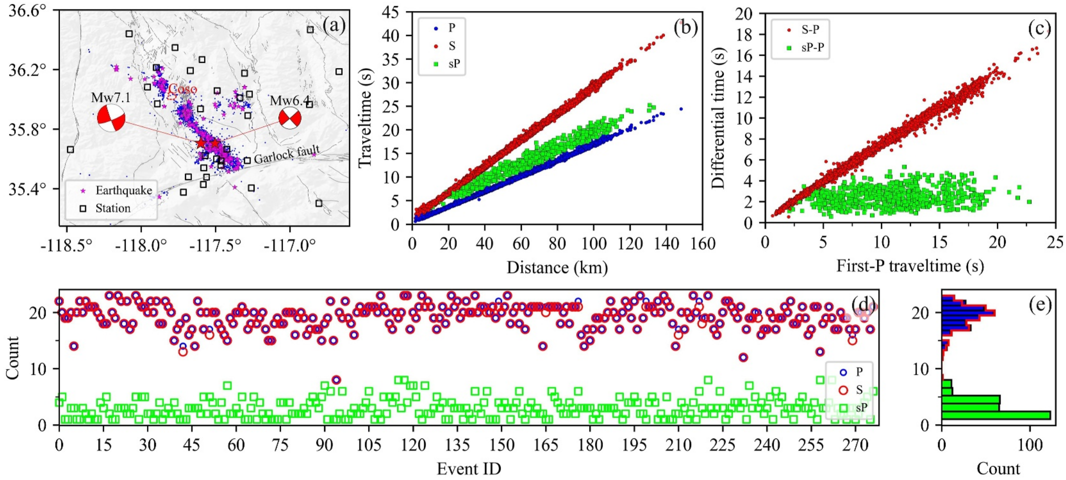

Figure 6. The obtained phase data in the Ridgecrest region, California. (a) Map view of the distribution of analyzed earthquakes (magenta stars) and the recording seismic stations (black open squares). Blue dots show the background seismicity. Red dashed line outlines the Coso geothermal site. (b) Traveltimes of first P (blue dots), S (red dots), and sP (lime squares) waves versus the epicentral distances. (c) A Wadati diagram showing the S-P (red dots) and sP-P (lime squares) arrival times versus first-P traveltimes. (d) The number of picked first P (blue open circle), S (red open circle) and sP (lime open square) phase data for each earthquake. (e) The statistic distribution of the picked phase data.

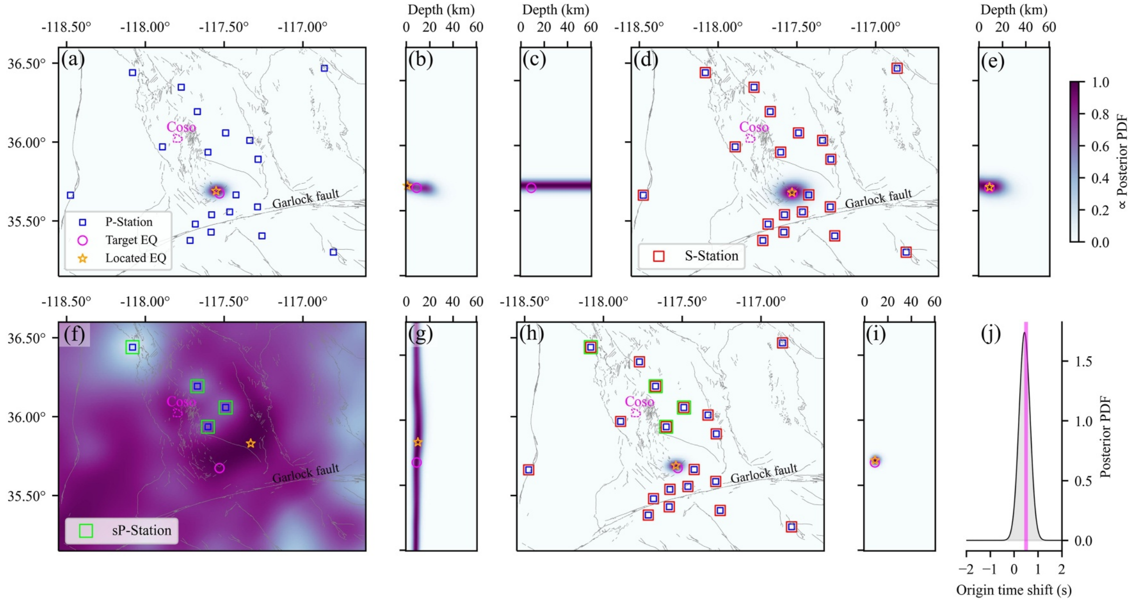

Figure 7. Three-step procedure to refine the earthquake hypocenter and its origin time. (a, b) The posterior probability density function (PDF) of earthquake hypocenter using only the first-P traveltimes in map and vertical profile views. Here, the phase traveltimes are numerically calculated within a 3D velocity model, and a Gaussian noise with 0.5-s mean and 0.1-s standard deviation is added to form the synthetic observations. The blue squares denote the seismic stations which provide first-P traveltimes. The star and circle represent the true and located earthquake hypocenter, respectively. (c) The modified earthquake hypocenter PDF which is homogeneous along the depth direction. (d, e) Are the same as (a, b) but for the posterior PDF of earthquake hypocenter using only the S-P differential arrival times. The open red squares denote the seismic stations which provide S-wave traveltimes. (f, g) Are the same as (a, b) but for the posterior PDF of earthquake hypocenter using only the sP-P differential arrival times. The open lime squares denote the seismic stations which provide sP traveltimes. (h, i) Are the same as (a, b) but for the posterior PDF of earthquake hypocenter using first-P traveltimes, and the S-P, sP-P differential arrival times together. (j) The posterior PDF of earthquake origin time shift by fitting first-P traveltimes. The red line denotes the true origin time shift (the mean of the added Gaussian noise).

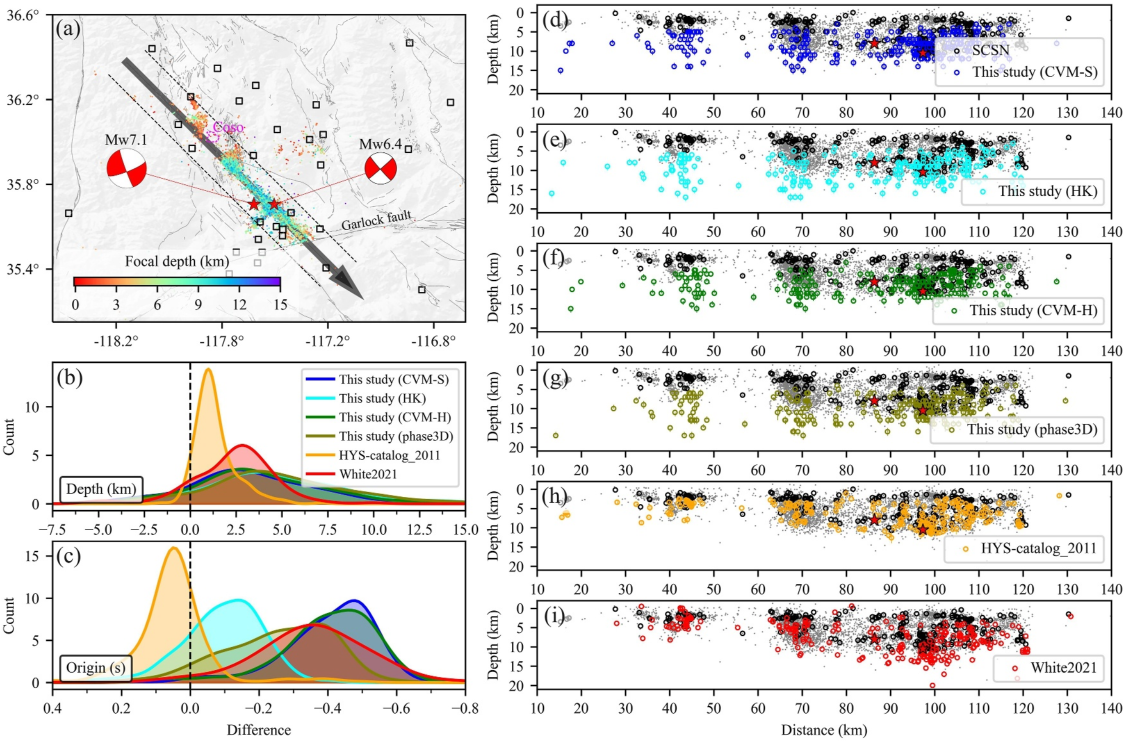

Figure 8. The comparison between our refined earthquake locations and other available earthquake catalogs in the Ridgecrest region. (a) The depth color-coded dots show the background seismicity. The open squares denote the utilized seismic stations when carrying out earthquake location in this study. The bold black arrow line trending NW-SE shows the position of vertical profile, in accordance with the Paxton Ranch fault zone (Thompson Jobe et al., 2020). Two black dashed lines, situated 10 km from the vertical profile, delineate the region within which earthquakes are projected onto the profile. (b) The differences of earthquake depths between the relocated results and the Southern California Seismic Network (SCSN) catalog. The relocated catalogs include our relocated results which are determined using first-P traveltimes, S-P and sP-P differential arrival times within either the CVM-S4.26 model (in blue), the HK model (in cyan), the CVM-H15.1.1 model (in green), or the phase3D model (in olive), the double-difference relocated catalog by Hauksson et al. (2012) (in orange), and the local catalog by White et al. (2021) (in red). (c) Is the same as (b) but for earthquake origin time shift. (d) Shows the background seismicity (gray dots), SCSN catalog (black open circles) and our relocated result (colored open circles) in vertical profile, where the present events are located no more than 10 km from the profile. The location uncertainty (vertical bar) of our result is obtained by projecting the location probability density function with normalized probability >0.95 onto the vertical profile. (e) Is the same as (c) but for the earthquake location results obtained in the HK model. (f) Is the same as (c) but for the earthquake location results obtained in the CVM-H15.1.1 model. (g) Is the same as (c) but for the earthquake location results obtained in the phase3D model. (h) The double-difference relocated catalog by Hauksson et al. (2012) with location uncertainties shown as vertical bars. (i) The local catalog by White et al. (2021).

(Figures 6a–6c). For these earthquakes, we have collected 5,350 first-arriving P-wave picks, and 5,338 first-arriving S-wave picks. On average, there are 19 P-wave picks, 19 S-wave picks, and 3 sP-wave picks per earthquake (Figure 6d). For first arrivals, the average azimuthal data coverage gap is 78.7° (Figure S16b in Supporting Information S1), and the nearest observation is, on average, 9.6 km away from the target event (Figure S18c in Supporting Information S1). The Wadati diagram of S-P and sP-P differential arrival times versus first P traveltimes shows a linear correlation (Figure 6c), underscoring the robustness of our phase data.

Now, we apply the newly developed earthquake location algorithm to the prepared phase data to refine the hypocenters and origin times of those 277 aftershocks, using first P arrival times, S-P and sP-P differential arrival times in the 3D CVM-S4.26 model. Results show that our refined earthquake epicenters closely align with the standard SCSN catalog with an average difference of 1.7 km (Figure S19a in Supporting Information S1), yet the earthquake depths exhibit a general increase of 3.8 km (Figure 8b, Figure S19b in Supporting Information S1), and the origin times tend to be 0.41 s earlier on average (Figures 8c, Figure S19c in Supporting Information S1). It is important to note that these generally deeper focal depths persist regardless of the type of phase data utilized (Figure S20 in Supporting Information S1). Additionally, the generally deeper earthquake foci than the SCSN catalog remain consistent across various existing catalogs, such as the relocated double-difference catalog by Hauksson et al. (2012) (Figures 8b and 8f), the relocated absolute earthquake catalog with station corrections by Lomax (2020), the local earthquake catalog constructed using a temporarily installed dense seismic array by

White et al. (2021) (Figures 8b and 8g), and the moment tensor catalog built with 3D Green's Functions by Wang and Zhan (2020). These catalogs span varied time periods of the 2019 Ridgecrest earthquake sequence; thus, our relocated deeper foci should not be a temporary phenomenon after the M_w 7.1 mainshock caused by either a transient higher strain rate in the lower crust (Ben-Zion & Lyakhovsky, 2006; Cheng & Ben-Zion, 2020) or the temporal velocity reduction which mainly occurred in the fault zone at shallow depths (Lu & Ben-Zion, 2022). Next, we discuss factors that may bias event depth during earthquake location and highlight the importance of accurate earthquake location depth in analyzing the local seismogenic processes.

5. Discussion

5.1. Factors Affecting Earthquake Depth Accuracy

In general, factors such as the azimuthal coverage of seismic stations, epicentral distances of seismic stations, phase picking uncertainties, and errors in the velocity model influence the accuracy of earthquake locations (e.g., Gomberg et al., 1990; Havskov et al., 2012). For our collected phase data, such as first arrivals, the average azimuthal gap is 78.7° (Figure 8b), and the average distance from the target event to the nearest observation is 9.6 km (Figure S18c in Supporting Information S1). This observational configuration provides solid foundation for the accurate earthquake localization. As for phase picking uncertainties, they have been carefully assessed using the AIC phase picker and incorporated into the location process within a Bayesian framework. Next, we evaluate the performances of earthquake location using various phase data combinations. To examine and mitigate the influence of velocity model errors on location accuracy, we conduct this evaluation across different velocity models.

In the Ridgecrest region, aftershocks located with first-P arrivals in the 3D CVM-S4.26 model show epicenters highly consistent with the SCSN catalog, with an average difference of 1.7 km. However, the computed focal depths are generally 4.4 km deeper, and the origin times are 0.37 s earlier on average (Figures S19a–S19c in Supporting Information S1). Interestingly, the relocated events tend to form a horizontal streak at around 9.0 km depth, with a standard deviation of 1.0 km (Figure S20a in Supporting Information S1). This streak pattern is likely an artifact resulting from a strong trade-off between event depth and origin time, and more details about the justification can be found in Text S5 and Figure S21 of Supporting Information S1.

Incorporating S-wave phase data, specifically S-P differential arrival times, into the earthquake location process reduces the horizontal streak artifact, resulting in an average source focus at 9.9 km depth with a standard deviation of 1.9 km (Figures S19b and S20c in Supporting Information S1). However, using S-P differential arrival times alone increases location uncertainties, particularly in the depth direction (Figure S20c in Supporting Information S1). By further including depth phase data, the relocated earthquake foci in the CVM-S4.26 model are more evenly distributed in the vertical direction, ranging from 3.0 to 15.0 km with a standard deviation of 2.8 km (Figures 8b–8d, Figures S19b, and S20e in Supporting Information S1). Additionally, the uncertainties in focal depth have been significantly reduced by more than a factor of five (Figure S20 in Supporting Information S1).

Locating earthquakes in other velocity models, such as the HK model, another 3D community velocity model, CVM-H15.1.1 (Shaw et al., 2015), and a 3D velocity model determined using phase arrival times (Fang et al., 2022; hereafter referred to as the phase3D model), could lead to different event foci, especially in terms of event depths (Figure S19 in Supporting Information S1). Specifically, when locating aftershocks with first-P arrivals, the event epicenters are quite stable, averaging no more than 1.7 km from the SCSN catalog across different velocity models like the CVM-S4.26, HK, and phase3D. The CVM-H15.1.1 model yields slightly farther epicenters, averaging about 2.1 km. The consistency of these horizontal location results indicates that the regular station coverage in the Ridgecrest region is effective to accurately locate earthquake epicenters. However, the situation is quite different for the focal depth determination. For instance, the obtained event foci in the HK model aligns closely with those from the SCSN catalog as expected. It presents an average 0.6-km difference in focal depth and a 0.10-s difference in origin time (Figures S19d–S19f in Supporting Information S1). While the determined depths in 3D velocity models like CVM-S4.26, CVM-H15.1.1, and phase3D are at least 2.6 km deeper on average. When locating aftershocks using S-P differential arrival times, the determined event foci across the four velocity models are more than 5.3 km deeper and origin times are at least 0.16 s earlier on average compared to the SCSN catalog. Notably, several events with relatively poor data coverage are biased toward either the surface or rather deep depths (Figure S20c in Supporting Information S1). When jointly using first arrivals and depth phases, we obtain more stable location results with the determined earthquake depths mostly

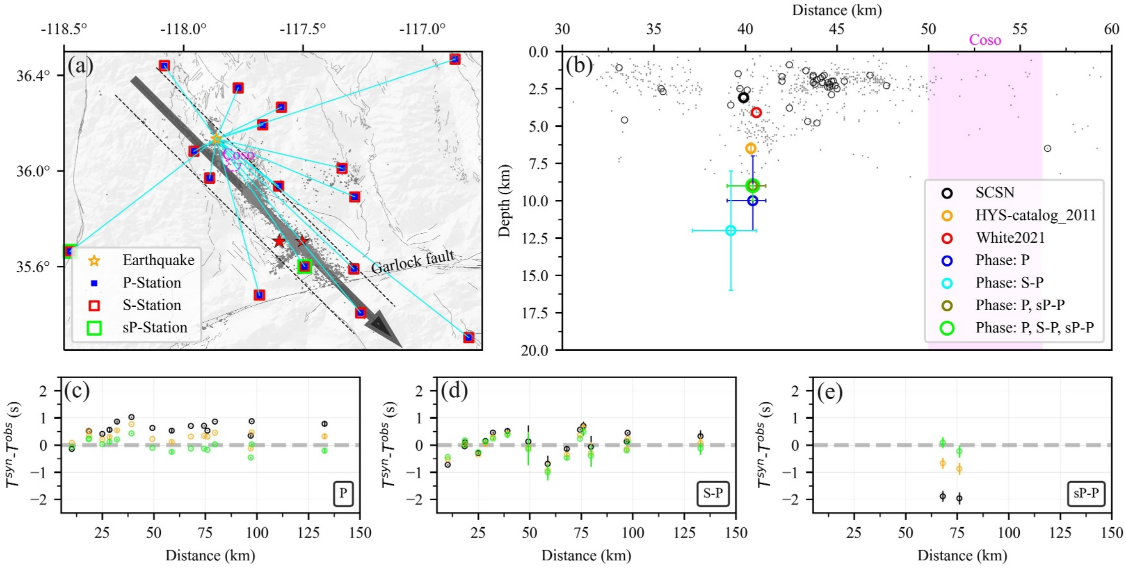

Figure 9. Verification of the deep event focus located to the northwest of the Coso geothermal site. (a) Map view of the test event which occurred on 2019-08-13T23:30:01.780000Z with a magnitude of 2.8 (orange open star) and the distribution of phase picking stations (squares). Blue, red open and lime open squares denote the seismic stations which provide first-P, S and sP traveltimes, respectively. Gray dots show the background seismicity. (b) The determined event foci in the vertical profile. Black bold circle shows the Southern California Seismic Network focus, whereas the orange circle denotes the double-difference relocated event focus by Hauksson et al. (2012), with its depth uncertainty displayed. Red circle presents the relocated event focus by White et al. (2021). The blue, cyan, olive and lime circles represent our relocated event foci within the CVM-S4.26 model via first-P arrival times, S-P differential arrival times, the joint use of first-P arrivals and sP-P differential times, and the joint use of first-P arrivals as well as S-P & sP-P differential arrival times. The location uncertainty is obtained by projecting the location probability density function with normalized probability >0.95 onto the vertical profile. (c) Shows the first-P traveltime residuals between the predicted and observed phase data versus epicentral distances. The three-standard-deviation interval of phase picking is also displayed as vertical bar. Here the predicted phase data are obtained in the CVM-S4.26 model using three different earthquake depths, where the color code aligns with the result shown in (b). (d) Is the same as (c) but for the S-P differential arrival time residuals. (e) Is the same as (c) but for the sP-P differential arrival time residuals.

comparable within 3 km (97.8%) across the four velocity models. The less dependence on velocity model indicates the improved accuracy in focal depth estimation with the inclusion of depth phases.

5.2. Deep Seismicity to the Northwest of Mainshock Epicenter

In this work, over 89% of the relocated earthquakes are found to be deeper than their reported locations in the SCSN catalog (Figure 8b). A detailed comparison of our relocated earthquake hypocenters with the double-difference catalog by Hauksson et al. (2012) and the local catalog constructed using a temporarily installed dense seismic array by White et al. (2021) shows that they all display the same trend of deeper earthquake foci compared to the SCSN catalog (Figures 8b and 8d–8i). However, discrepancies in earthquake depths are also evident. For example, along the NW-SE fault trace beneath the Paxton Ranch fault zone (Thompson Jobe et al., 2020), our relocated earthquake depths are on average 4.0 km deeper near the 45 km segment and 3.1 km deeper near the 70 km segment than those in both the double-difference catalog by Hauksson et al. (2012) and the local catalog by White et al. (2021). While in the 90 km segment near the mainshock epicenter, our determined earthquake depths fall averagely in between the estimates by the two catalogs. Generally, our location result aligns better with the local catalog by White et al. (2021) in the mainshock epicenter area, where most rapid-response seismic stations were installed (e.g., Cochran et al., 2020; White et al., 2021).

To justify the reliability of our relocated greater event depths 10 km farther northwest of the mainshock region, we investigate the S-P phase traveltime fitting and the stacking prominence of sP waves using previous catalog foci and our relocated greater foci. Here we present the key points, and more details can be found in Text S6 in Supporting Information S1. Between the 40 and 50 km segment along the NW-SE fault trace, rare post-quake seismic stations were installed (e.g., Cochran et al., 2020; White et al., 2021). Our relocated greater event foci can best fit both the S-P phase arrivals at close stations (whose distance away from the event is less than 1-times our relocated depth), and the S-P phase arrivals across all available stations (Figures S22a and S22b in Supporting Information S1). The detailed phase traveltime fitting of one representative earthquake in the CVM-S4.26 model (Figure 9) further shows that our relocated greater focus best fit the arrivals of first P and sP waves. Meanwhile, the waveform stacking prominence is only significant near the sP arrivals using our relocated foci (Figures S22c and S22d in Supporting Information S1). The scenario is the same between the 90 and 110 km segment near the mainshock epicenter area (Figures S22i–S22l in Supporting Information S1), where most seismic stations were installed rapidly after the mainshock (e.g., Cochran et al., 2020; White et al., 2021). These demonstrate that our relocated greater depths to the northwest of the Coso geothermal site and near the mainshock epicenter area are reliable.

Between the 60 and 75 km segment along the NW-SE fault trace, there are some seismic stations installed rapidly after the mainshock (e.g., Cochran et al., 2020; White et al., 2021). Our relocated greater event foci can well or better fit the S-P phase arrivals across all available stations (Figures S22f, S23d, S23h, S23l, and S23p in Supporting Information S1), while we also observe that shallower event foci can better fit the S-P phase arrivals at close stations (Figures S22e, S23c, S23g, S23k, and S23o in Supporting Information S1). Such contradictory inference on the earthquake depth between close stations and all available stations is different from the cases in other segments along the NW-SE profile (Figures S22a, S22b, S22i, and S22j in Supporting Information S1). Given the accurate phase picking (Figure S5 in Supporting Information S1) and constructive sP waveform stacking using our greater relocated event foci (Figures S22g and S22h in Supporting Information S1), we speculate that some unmapped localized structures could exist in the rupture termination area of the mainshock (e.g., Yeh & Olsen, 2023; Zhou et al., 2022), which would bias the phase traveltimes at close stations. If close station observations were strongly affected by localized velocity heterogeneities, then any inference from close observations on the source properties using a regional velocity model would need to be double-checked.

5.3. Implications for Behaviors of Large Earthquakes

Accurate determination of small earthquake hypocenters allows for a reliable estimation of the depth range of the seismogenic zone within the crust, thus providing valuable insights into the behaviors of large earthquakes. For instance, in the Ridgecrest region, a significant shallow slip deficit during the 2019 earthquake sequence has been observed, reaching up to 20% according to data-assimilated dynamic modeling (Taufiqurrahman et al., 2023), or even exceeding 60% based on a kinematic inversion using multiple data sets (Qiu et al., 2020). Our relocated results using first arrivals and depth phases show few aftershocks occurred above 3 km depth beneath the northwest-trending Paxton Ranch fault zone, reinforcing a lack of shallow aftershocks noted in previous studies (Hauksson & Jones, 2020; Lomax, 2020). Given the good spatial correlation between the aseismic shallow crust and the low velocity zone imaged by an ambient noise tomography model with densely deployed nodes (Zhou et al., 2022), we propose that the aseismic region of the uppermost crust above 3 km depth represents a weak fault damage zone, and is responsible for the observed shallow slip deficit during the 2019 Ridgecrest earthquake sequence (Roten et al., 2017).

The lower limit of the seismogenic zone is usually inferred based on the depth distribution of local seismicity. Here, we define the lower limit of a seismogenic zone as the depth above which 95% of crustal earthquakes have occurred, following previous studies (e.g., Nazareth & Hauksson, 2004; Zuza & Cao, 2020), and refer to it as the D95 depth. The uncertainty of a D95 estimate is characterized by the RMS of the depth differences between D95 and the earthquakes below it. To account for location errors stemming from velocity model uncertainties, we introduce a composite D95 depth, calculated as the average of D95 estimates obtained from four different velocity models. Its upper bound corresponds to the shallowest D95, while the lower bound reflects the deepest D95 estimate. The M_w 6.4 foreshock nucleated at a depth of 10.5 km according to the SCSN catalog, or even deeper at 12 km depth as reported by Lomax (2020). This depth is intriguing as it already surpasses the lower limit of the local seismogenic zone, as defined by the SCSN catalog. Notably, the foreshock nucleation depth aligns closely with the base of our determined seismogenic zone at around 12.8 km depth (Figures 10b and 10d). This is consistent with the fact that large earthquakes ($M > 5.5$) often nucleate near the base of the seismogenic zone, where the distortion strain energy is thought to be most highly concentrated (Das & Scholz, 1983; Huc et al., 1998; Sibson, 1982). In contrast, the M_w 7.1 mainshock nucleated unexpectedly at a shallower depth of 8.0 km according to the SCSN catalog, or even shallower at around 4 km depth as reported by Lomax (2020). Regardless, the rupture initiated at a depth obviously above the base of our determined seismogenic zone (around 14.5 km at depth, Figure 10d) is uncommon. The presence of heterogeneities, such as the local over-pressurized conditions, could have facilitated the nucleation of the M_w 7.1 mainshock at such a shallow depth and promoted the subsequent rupture propagation throughout the entire seismogenic zone (Das & Scholz, 1983; Taufiqurrahman et al., 2023; Tong et al., 2021).

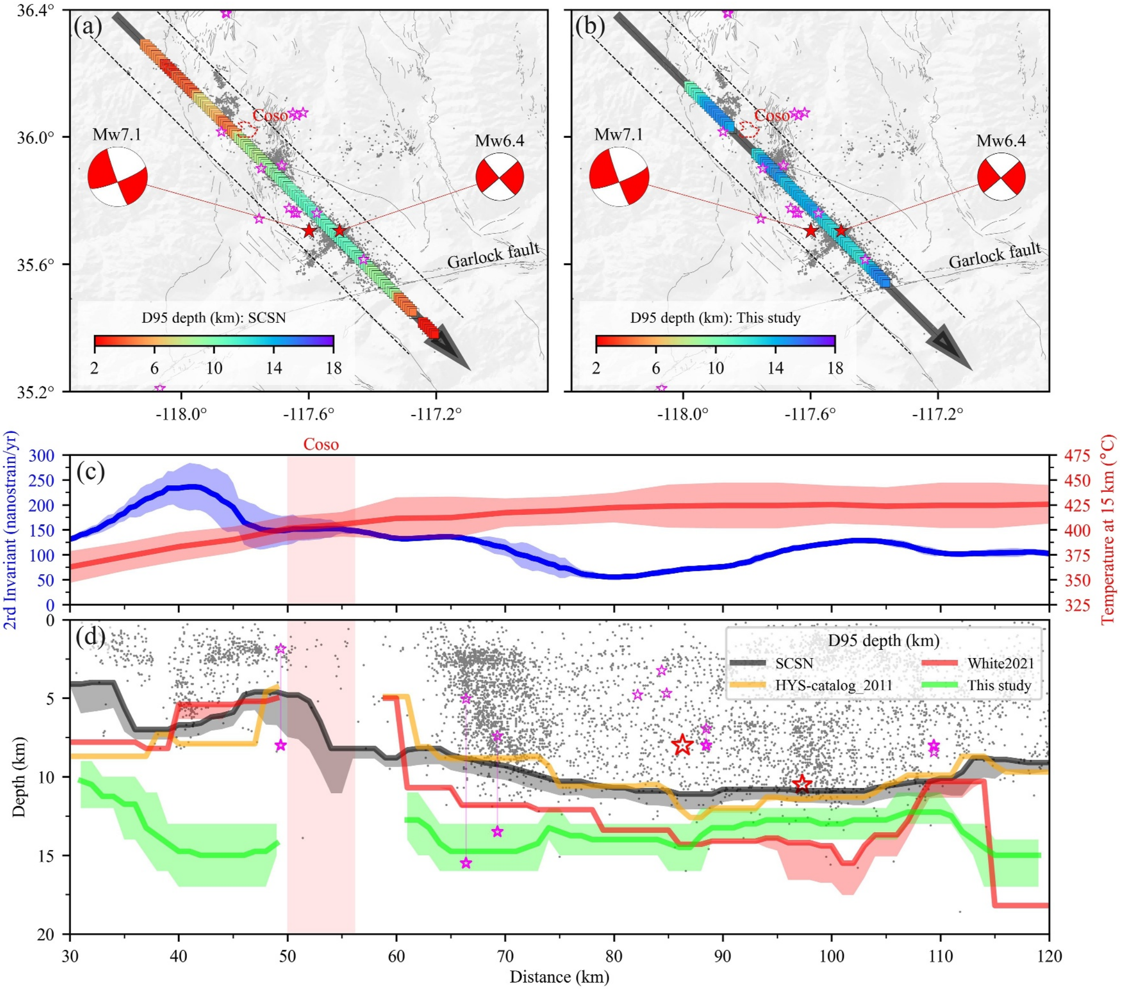

Figure 10. 2D seismogenic zone structure beneath the Paxton Ranch fault zone in the Ridgecrest region. (a) The lower limit of seismogenic zone (D95). Gray dots show the background seismicity, and they are used to calculate the Southern California Seismic Network (SCSN) D95 values. Magenta stars denote the event focus with magnitude larger than 5.0 since 1980 according to the ANSS Comprehensive Earthquake Catalog. (b) Is the same as (a) but using our relocated results using first arrivals and depth phases within four different velocity models to calculate a composite D95 depth. (c) Along the profile, the second invariant strain rate with three-standard-deviation interval (blue curve) is derived from the SCEC community geodetic model (Sandwell et al., 2016). The middle crust (15 km depth) temperature with three-standard-deviation interval (red curve) is extracted from the SCEC community temperature model (Shinevar et al., 2018). (d) D95 depths inferred from the SCSN catalog (in black), the double-difference catalog (in orange, Hauksson et al., 2012), and the local catalog by (in red, White et al., 2021). The composite D95 depths inferred from our relocated results using both first arrivals and depth phases across four different velocity models are shown in lime. Magenta stars denote the earthquake hypocenters with magnitude greater than 5.0 since 1980, while the bold stars represent the centroid-moment centers according to the ANSS ComCat.

In two segments along the NW–SE profile at approximate distances of 45 and 70 km, the base of our determined seismogenic zone is unprecedentedly about 7.1 and 2.9 km deeper, respectively, than that inferred from existing catalogs (Figure 10d). For strike-slip faults, a thicker seismogenic zone has a higher potential for generating large magnitude events (e.g., Weng & Yang, 2017), implying that the potential for large earthquakes greater than M5.5 in these sections should not be overlooked. In fact, within just 1 hour after the M_w 7.1 mainshock, two earthquakes with magnitudes greater than 5.4 occurred approximately 20 km away to the northwest. Their hypocenters are located shallower than 7.5 km, whereas their centroid depths exceed 13.5 km according to the ANSS Comprehensive Earthquake Catalog (ComCat, US Geological Survey, 2017). This surpasses the local D95 depth based on existing catalogs but remains above the lower bound of our composite D95 depth (Figure 10d). To the northwest of the Coso geothermal site, near the distance of 49 km along the NW-SE profile, a M5.2 earthquake occurred in 2001 with a very shallow hypocenter at around 1.9 km, whereas its centroid depth is estimated at 8.0 km exceeding the local D95 depths from existing catalogs. Although we cannot constrain the D95 depth in that area due to the temporally weak seismicity (Text S7 and Figure S24 in Supporting Information S1), our nearest D95 depth estimate is 14.3 km. This unprecedented deep D95 estimate is consistent with the local high strain rate observed by Sandwell et al. (2016) and relatively low temperature in the middle crust reported by Shinevar et al. (2018) (Zuza & Cao, 2020, Figure 10c). Following the trend of shallower D95 depths to the southeast, the D95 depth just northwest of the Coso geothermal site is likely to remain above 10.0 km (Figure 10d). According to the long-term near-site catalog, the Coso geothermal site is reported to have a locally rather shallow brittle-to-ductile transition zone above 4.0 km depth (Monastero et al., 2005). The abrupt change of local D95 depths across the geothermal site may act as a rheological barrier (Im et al., 2021), potentially modulating the rupture propagation of large earthquakes.

6. Conclusions

In this study, we designed an integrative procedure to identify the depth phase sP on local and regional seismic records. Subsequently, we updated earthquake locations within a Bayesian inversion framework. Our case study in the Ridgecrest region of California highlights that the standard SCSN catalog tends to locate earthquakes at shallower depths. This discrepancy arises from the reliance on first-P arrival times for locating earthquakes, which often suffers the severe trade-off between event depth and origin time. This issue is exacerbated when horizontal velocity heterogeneities are not adequately considered during the location process (Hutton et al., 2010). Our results show earthquake foci at depths comparable to the existing relocated catalogs beneath the mainshock area, where dense seismic node arrays were rapidly instrumented after the mainshock. While aside from the Coso geothermal site, our findings reveal a generally deeper brittle-to-ductile zone to the northwest of the mainshock nucleation region. Focal depth discrepancies across different earthquake catalogs, particularly in regions lacking dense local station coverage, highlight the need for improved earthquake location methodologies in future studies. In such cases, local depth phases could play a key role in reducing uncertainty in focal depth estimates.

In this work, we address velocity model uncertainty by carrying out earthquake location in four different velocity models. However, the effect of velocity model uncertainty is not included in any single posterior probability density function (PDF). Future work should explore methods to incorporate velocity model uncertainty into a unified posterior PDF, potentially through stochastic location sampling across differesnt velocity models (e.g., Myers et al., 2007). Continued efforts should also aim to build a comprehensive earthquake catalog refined using depth phase data, both in the Ridgecrest region and across California. Such a catalog would enable the investigation of spatiotemporal variations in the seismogenic zone, for example, transient variations in D95 depths as observed beneath the Coso geothermal site after the 2019 M_w 7.1 earthquake (Figure S24 in Supporting Information S1). Furthermore, a local sP waveform database could be leveraged to develop data-driven AI tools (Münchmeyer et al., 2024) in the future.

Appendix A: Bayesian Inversion for Locating Earthquakes

In earthquake location, our objective is to constrain $\boldsymbol{m} = (\boldsymbol{x}, \tau)$ which comprises three spatial coordinates representing the hypocenter (longitude, latitude, depth denoted as $\boldsymbol{x} = (\theta, \phi, z)$), and an origin time τ, based on the observed data $\boldsymbol{d}$. The data may include traveltimes of first-arriving P or/and S waves, as well as depth phase (sP), and is related to the model parameters through a theoretical relationship $\Theta(\boldsymbol{d}, \boldsymbol{m})$. In this study, $\Theta(\boldsymbol{d}, \boldsymbol{m})$ strictly follows the eikonal equation (e.g., Rawlinson & Sambridge, 2005) and can be expressed in a symbolic form as $\boldsymbol{d} = g(\boldsymbol{m})$. Under the Bayesian inversion framework, our goal is to update our knowledge about earthquake hypocenter and origin time from the prior distribution $\rho(\boldsymbol{m})$ to the posterior distribution $\sigma(\boldsymbol{m})$ by incorporating the information gained from the observations $\boldsymbol{d}$ (Sambridge & Mosegaard, 2002):

$$\sigma(\boldsymbol{m}) = k\rho(\boldsymbol{m})\, L(\boldsymbol{m}), \tag{A1}$$

where k is a normalization constant, and $L(\boldsymbol{m})$ is the likelihood. Following Sambridge and Mosegaard (2002), a typical likelihood function can be expressed as:

$$L(\boldsymbol{m}) = e^{-S(\boldsymbol{m})}, \tag{A2}$$

where the misfit $S(\boldsymbol{m})$ can be written in a general expression (Tarantola, 2005):

$$S(\boldsymbol{m}) = \frac{1}{p}\left(\sum_i \frac{\left(d^i_{\text{obs}} - g^i(\boldsymbol{m})\right)^p}{\left(C^i\right)^p}\right), \tag{A3}$$

Here the variable $i \in [1,2,3,\cdots,N]$ denotes the i-th traveltime of the total N observations, and C^i refers to the uncertainty of the i-th observation d^i_{obs}. Note that here we neglect the uncertainty related to the model's prediction compared to the original formula given by Tarantola (2005). In Equation A3, the uncertainty term related to observations in the denominator serves as a weighting parameter: a smaller uncertainty results in a greater weight, and vice versa. In light of this fact, we use specifically designed weighting parameters in this study.

As there is usually a strong trade-off between earthquake origin time and focal depth (Gomberg et al., 1990), we adopt a three-step inversion strategy to determine the four-dimensional earthquake location $\boldsymbol{m} = (\boldsymbol{x}, \tau)$. First, we utilize the first-P traveltimes, which typically have better azimuthal coverage than other observations (e.g., first S or later phases), to infer the earthquake hypocenter $\boldsymbol{x}$ (mainly the epicenter). In this step, we assume a prior uniform distribution $\rho_1(\boldsymbol{x}, \tau_0) = \text{constant}$ for the hypocenter, where the origin time is fixed as τ_0 from the standard catalog. And we apply a composite weighting scheme to the first-P traveltimes, which consists of two parts:

$$\omega^i_{\text{comp}} = \underbrace{1/\max\left(t^i_{\text{std}}, t_{\text{delta}}\right)}_{\text{picking uncertainty}} \cdot \underbrace{1/\sum\nolimits_j e^{-\left(\frac{\Delta_{\text{ij}}}{\Delta_{\text{ref}}}\right)^2}}_{\text{station geometry}}, \tag{A4}$$

The first part addresses picking uncertainty. t^i_{std} represents the picking error of the i-th observation, which is replaced by t_{delta}, the seismogram's sampling interval, if $t^i_{\text{std}} < t_{\text{delta}}$. The general effect of the first part is to emphasize the picks with smaller picking uncertainties while reducing the influence of potential outliers in the misfit function. The second part relates to the station geometry, where Δ_{ij} refers to the inter-station distance between the i-th and j-th stations, and Δ_{ref} is a reference distance used to balance the ratio of maximum to minimum weights. It serves as a declustering operator, ensuring equal contributions from all azimuths and helping produce an unbiased earthquake epicenter (Ruan et al., 2019). In our study, we fix Δ^{ref} at 50 km for local and regional observations. We use a normalized weighting coefficient $\frac{\sqrt{N} \cdot \omega^i_{\text{comp}}}{\sum_{j=1}^N \omega^j_{\text{comp}}}$ as the uncertainty term $\left(1/C^i\right)^p$ in Equation A3, yielding the posterior probability density function (PDF) of the earthquake hypocenter $\boldsymbol{x}$ in the first step:

$$\sigma_1(\boldsymbol{x}; \tau_0) = k_1 \rho_1(\boldsymbol{x}, \tau_0)\, e^{-\frac{1}{2}\left(\sum_{i=1}^N\left(\frac{\sqrt{N} \cdot \omega^i_{\text{comp}}\left(d^i_P - g^i(\boldsymbol{x}; \tau_0)\right)^2}{\sum_{j=1}^N \omega^j_{\text{comp}}}\right)\right)}, \tag{A5}$$

where the misfit between the model's prediction and observation is measured using the L_2 norm. N refers to the total number of the first P traveltimes used in forming the misfit function, and $\sqrt{N}$ is included in the numerator of the normalized weighting coefficient to compensate for the information loss (see further discussion in Text S4 and Figure S25 of Supporting Information S1). The constant k_1 is introduced to ensure that $\sigma_1(\boldsymbol{x}; \tau_0)$ is a valid PDF. The same applies to the constants m_1, k_2 and k_3, which are introduced later. At this step, the approximate earthquake hypocenter $\boldsymbol{x}$ is determined:

$$(\theta^*, \phi^*, z^*) = \underset{\theta,\phi,z}{\operatorname{argmax}}\, \sigma_1(\theta, \phi, z; \tau_0), \tag{A6}$$

Since first P waves are typically the most abundant observations with good azimuthal coverage, the estimated earthquake epicenter (θ^*, ϕ^*) is generally more reliable compared to the focal depth z^*, which often suffers a serious trade-off between the earthquake depth and origin time.

In the second step, we modify the earthquake hypocenter PDF $\sigma_1(\boldsymbol{x}; \tau_0)$ to make it homogeneous along the depth direction (Figures 7a–7c), and use the modified version as the prior distribution for the earthquake hypocenter:

$$\rho_2(\theta, \phi, z; \tau_0) = m_1 \sigma_1(\theta, \phi, z^*; \tau_0), \tag{A7}$$

We form the posterior PDF for the earthquake hypocenter $\boldsymbol{x}$ at the second step by involving the S-P and sP-P differential arrival times:

$$\sigma_2(\boldsymbol{x}; \tau_0) = k_2 \rho_2(\boldsymbol{x}; \tau_0)\, e^{-\left(\frac{1}{2}\sum_{i=1}^{N_{S-P}}\left(\frac{\sqrt{N_{S-P}}\cdot\omega_{\mathrm{comp}}^{i}\left(d_{S-P}^{i}-g^{i}(\boldsymbol{x};\tau_0)\right)^2}{\sum_{j=1}^{N_{S-P}}\omega_{\mathrm{comp}}^{j}}\right)+\frac{1}{2}\sum_{l=1}^{N_{sP-P}}\left(\frac{\sqrt{N_{sP-P}}\cdot\omega_{\mathrm{comp}}^{l}\left(d_{sP-P}^{l}-g^{l}(\boldsymbol{x};\tau_0)\right)^2}{\sum_{j=1}^{N_{sP-P}}\omega_{\mathrm{comp}}^{j}}\right)\right)}, \tag{A8}$$

where N_{S-P} represents the number of S-P differential arrival times used, and N_{sP-P} denotes the number of sP-P differential arrival times. Importantly, the inferred earthquake location is independent of the origin time (Figures 7d–7i) due to the use of differential arrival times. The involvement of depth phase sP waves further reduces the location uncertainty along the depth direction (Figures 7f–7i).

In the third and last step, we use the maximum likelihood estimate of the earthquake hypocenter

$$\hat{\boldsymbol{x}} = \underset{\boldsymbol{x}}{\operatorname{argmax}}\ \sigma_2(\boldsymbol{x}; \tau_0), \tag{A9}$$

to predict the first-P traveltimes, refining the earthquake origin time τ by fitting those observations (Figure 7j):

$$\sigma_3(\tau; \hat{\boldsymbol{x}}) = k_3 \rho_3(\boldsymbol{x}, \tau_0)\, e^{-\frac{1}{2}\left(\sum_{i=1}^{N}\left(\frac{\sqrt{N}\cdot\omega_{\mathrm{std}}^{i}\left(d_{P}^{i}-g^{i}(\tau;\ \hat{\boldsymbol{x}})\right)^2}{\sum_{j=1}^{N}\omega_{\mathrm{std}}^{j}}\right)\right)}, \tag{A10}$$

Note that we assume a prior uniform distribution $\rho_3(\boldsymbol{x}, \tau_0) = constant$ for the origin time and use only the picking uncertainty-related weighting scheme $\omega_{\mathrm{std}}^{i}$ (the first part of Equation A4). From the perspective of dealing with error terms, we argue that the obtained posterior PDFs offer a more comprehensive characterization of the earthquake hypocenter and its origin time. This is because we have accounted for both the systematic errors arising from the overly simplified background velocity model (we use a 3D background velocity model), uneven station distribution (we apply a geographic weighting scheme), and the random errors related to the phase picking (we use a picking uncertainty-related weighting scheme). From these posterior PDFs, we can derive various types of information regarding the model parameters, including mean values, median values, maximum likelihood estimates, and uncertainty bars (Tarantola, 2005).

To provide a more concise assessment, following the methodology of Lomax et al. (2009), we will also employ seven quality indicators to evaluate the reliability and precision of the earthquake location results (Figures S18 and S26 in Supporting Information S1). These indicators include the picking error-weighted RMS of traveltime residuals (rms), the largest angle between the epicenter and two azimuthally adjacent seismic stations (gap), the distance from the epicenter to the nearest seismic station (Δ_0), the number of observations used in the location (N), and the half-lengths of the three principal axes of a 90% confidence error ellipsoid approximating the posterior PDF of the earthquake hypocenter ($I_{\mathrm{ell}}^{1} \geq I_{\mathrm{ell}}^{2} \geq I_{\mathrm{ell}}^{3}$). We utilize principal component analysis to determine these three principal axes and subsequently update their half-lengths while maintaining a fixed ratio of their eigenvalues until the accumulated probability within the ellipsoid approaches 0.9.

To improve the efficiency of earthquake location using the above three-step procedure, we precompute traveltime fields for the first-arriving P, S waves, and depth phase sP waves by numerically solving the eikonal equation, applying the source-receiver reciprocity theorem. These traveltime fields are stored for reuse in subsequent calculations. This approach ensures that the computational cost of forward traveltime modeling is proportional to the number of seismic stations, independent of the number of potential earthquakes. This is particularly effective in regions with stable seismic networks.

Conflict of Interest

The authors declare no conflicts of interest relevant to this study.

Data Availability Statement

In this work, the analyzed seismic event waveforms are provided by the Caltech/USGS SCSN (https://doi.org/10.7914/SN/CI; California Institute of Technology (Caltech), 1926) and its collaborative partner networks including RAPID: Capturing aftershock sequence of 2019 M_w 6.4 Ridgecrest and 7.1 Ridgecrest earthquakes (RAPID Ridgecrest) (7Q, https://doi.org/10.7914/SN/7Q_2019; Ghosh, 2019), US Geological Survey Networks (GS, https://doi.org/10.7914/SN/GS; Albuquerque Seismological Laboratory (ASL)/USGS, 1980), Nevada Seismic Network (NN, https://doi.org/10.7914/SN/NN; University of Nevada, Reno, 1971), and Plate Boundary Observatory Borehole Seismic Network (PB, available at https://www.fdsn.org/networks/detail/PB/). The data are stored at the Southern California Earthquake Data Center (SCEDC, https://doi.org/10.7909/C3WD3xH1; SCEDC, 2013). Catalog location of the analyzed earthquakes between 1 August and 30 September 2019, as well as the event hypocenters and magnitudes for the background seismicity between 5 June and 30 September 2019 are obtained from the Caltech/USGS southern California earthquake catalog (Hutton et al., 2010). Focal mechanisms of the M6.4 foreshock and M7.1 mainshock, as well as available seismic phase data (first-arriving P, S traveltimes) are retrieved from the SCEDC (2013). The centroid depths of the earthquakes with magnitude greater than 5.0 since 1980 are extracted from the ANSS Comprehensive Earthquake Catalog (ComCat, https://doi.org/10.5066/F7MS3QZH; US Geological Survey, 2017). The utilized first P, S and sP phase data, and the refined earthquake hypocenters and origins in this study can be accessed at (https://doi.org/10.21979/N9/BHCBP6; Tong, 2024). Figures are made with Matplotlib (Hunter, 2007) and PyGMT (Tian et al., 2025). ObsPy (Beyreuther et al., 2010) and Scipy (Virtanen et al., 2020) are used when downloading and processing seismic data.

Acknowledgments

The authors are grateful to Editor Rachel Abercrombie, an associate editor and three anonymous reviewers for time and efforts they spent in evaluating this manuscript. Their constructive comments and suggestions have greatly improved the manuscript quality. This work is supported by the Ministry of Education, Singapore, under its MOE AcRF Tier-1 Grant (RG97/24) and its MOE AcRF Tier-2 Grant (MOE-T2EP20124-0003). X. Yang is partially supported by the NSF Grant DMS-2109116. The SCEDC and SCSN are funded through U.S. Geological Survey Grant G20AP00037, and the Southern California Earthquake Center, which is funded by NSF Cooperative Agreement EAR-0529922 and USGS Cooperative Agreement 07HQAG0008.

References

Aki, K., & Richards, P. G. (2002). *Quantitative seismology*. MIT Press.

Albuquerque Seismological Laboratory (ASL)/USGS. (1980). *US Geological Survey networks*. International Federation of Digital Seismograph Networks. https://doi.org/10.7914/SN/GS

Armstrong, A. D., Claerhout, Z., Baker, B., & Koper, K. D. (2023). A deep-learning phase picker with calibrated Bayesian-derived uncertainties for earthquakes in the Yellowstone volcanic region. *Bulletin of the Seismological Society of America*, *113*(6), 2323–2344. https://doi.org/10.1785/0120230068

Ben-Zion, Y., & Lyakhovsky, V. (2006). Analysis of aftershocks in a lithospheric model with seismogenic zone governed by damage rheology. *Geophysical Journal International*, *165*(1), 197–210. https://doi.org/10.1111/j.1365-246x.2006.02878.x

Beyreuther, M., Barsch, R., Krischer, L., Megies, T., Behr, Y., & Wassermann, J. (2010). ObsPy: A Python toolbox for seismology. *Seismological Research Letters*, *81*(3), 530–533. https://doi.org/10.1785/gssrl.81.3.530

Bowers, D., & Selby, N. D. (2009). Forensic seismology and the comprehensive nuclear-test-ban treaty. *Annual Review of Earth and Planetary Sciences*, *37*(1), 209–236. https://doi.org/10.1146/annurev.earth.36.031207.124143

Branum, D., Harmsen, S., Kalkan, E., Petersen, M., & Wills, C. (2008). *Earthquake shaking potential for California*. California Geological Survey Map Sheet.48.

California Institute of Technology (Caltech). (1926). Southern California seismic network [Dataset]. *International Federation of Digital Seismograph Networks*. https://doi.org/10.7914/SN/CI

Cheng, Y., & Ben-Zion, Y. (2020). Variations of earthquake properties before, during, and after the 2019 M7. 1 Ridgecrest, CA, earthquake. *Geophysical Research Letters*, *47*(18), e2020GL089650. https://doi.org/10.1029/2020gl089650

Cochran, E. S., Wolin, E., McNamara, D. E., Yong, A., Wilson, D., Alvarez, M., et al. (2020). The US Geological Survey's rapid seismic array deployment for the 2019 Ridgecrest earthquake sequence. *Seismological Research Letters*, *91*(4), 1952–1960. https://doi.org/10.1785/0220190296

Craig, T. J. (2019). Accurate depth determination for moderate-magnitude earthquakes using global teleseismic data. *Journal of Geophysical Research: Solid Earth*, *124*(2), 1759–1780. https://doi.org/10.1029/2018jb016902

Das, S., & Scholz, C. H. (1983). Why large earthquakes do not nucleate at shallow depths. *Nature*, *305*(5935), 621–623. https://doi.org/10.1038/305621a0

Fang, H., White, M. C., Lu, Y., & Ben-Zion, Y. (2022). Seismic traveltime tomography of Southern California using poisson-voronoi cells and 20 years of data. *Journal of Geophysical Research: Solid Earth*, *127*(5), e2021JB023307. https://doi.org/10.1029/2021jb023307

Ghosh, A. (2019). RAPID: Capturing aftershock sequence of 2019 Mw 6.4 Ridgecrest and 7.1 Ridgecrest earthquakes. *International Federation of Digital Seismograph Networks*. https://doi.org/10.7914/SN/7Q_2019

Gomberg, J. S., Shedlock, K. M., & Roecker, S. W. (1990). The effect of S-wave arrival times on the accuracy of hypocenter estimation. *Bulletin of the Seismological Society of America*, *80*(6A), 1605–1628. https://doi.org/10.1785/bssa08006a1605

Hadley, D., & Kanamori, H. (1977). Seismic structure of the transverse ranges, California. *Geological Society of America Bulletin*, *88*(10), 1469–1478. https://doi.org/10.1130/0016-7606(1977)88<1469:ssottr>2.0.co;2

Hauksson, E., & Jones, L. M. (2020). Seismicity, stress state, and style of faulting of the Ridgecrest-Coso region from the 1930s to 2019: Seismotectonics of an evolving plate boundary segment. *Bulletin of the Seismological Society of America*, *110*(4), 1457–1473. https://doi.org/10.1785/0120200051

Hauksson, E., & Meier, M.-A. (2019). Applying depth distribution of seismicity to determine thermo-mechanical properties of the seismogenic crust in Southern California: Comparing lithotectonic blocks. *Pure and Applied Geophysics*, *176*(3), 1061–1081. https://doi.org/10.1007/s00024-018-1981-z

Hauksson, E., Yang, W., & Shearer, P. M. (2012). Waveform relocated earthquake catalog for Southern California (1981 to June 2011). *Bulletin of the Seismological Society of America*, *102*(5), 2239–2244. https://doi.org/10.1785/0120120010

Havskov, J., Bormann, P., & Schweitzer, J. (2012). Seismic source location. In *New manual of seismological observatory practice* (Vol. 2(NMSOP-2), pp. 1–36). Deutsches GeoForschungsZentrum GFZ.

He, X., Zhang, P., Ni, S., & Zheng, W. (2019). Resolving focal depth in sparse network with local depth phase sPL: A case study for the 2011 Mineral, Virginia, earthquake sequence. *Bulletin of the Seismological Society of America*, *109*(2), 745–755. https://doi.org/10.1785/0120180221

Huc, M., Hassani, R., & Chéry, J. (1998). Large earthquake nucleation associated with stress exchange between middle and upper crust. *Geophysical Research Letters*, *25*(4), 551–554. https://doi.org/10.1029/98gl00091

Hunter, J. D. (2007). Matplotlib: A 2D graphics environment. *Computing in Science & Engineering*, *9*(3), 90–95. https://doi.org/10.1109/mcse.2007.55

Hutton, K., Woessner, J., & Hauksson, E. (2010). Earthquake monitoring in Southern California for seventy-seven years (1932-2008). *Bulletin of the Seismological Society of America*, *100*(2), 423–446. https://doi.org/10.1785/0120090130

Im, K., Avouac, J.-P., Heimisson, E. R., & Elsworth, D. (2021). Ridgecrest aftershocks at Coso suppressed by thermal destressing. *Nature*, *595*(7865), 70–74. https://doi.org/10.1038/s41586-021-03601-4

Ji, C., Helmberger, D. V., Wald, D. J., & Ma, K.-F. (2003). Slip history and dynamic implications of the 1999 Chi-Chi, Taiwan, earthquake. *Journal of Geophysical Research*, *108*(B9). https://doi.org/10.1029/2002jb001764

Kirmse, A., & de Ferranti, J. (2017). Calculating the prominence and isolation of every mountain in the world. *Progress in Physical Geography*, *41*(6), 788–802. https://doi.org/10.1177/0309133317738163

Koper, K. D., Burlacu, R., Murray, R., Baker, B., Tibi, R., & Mueen, A. (2024). Inferring the focal depths of small earthquakes in southern California using physics-based waveform features. *Bulletin of the Seismological Society of America*, *114*(5), 2376–2396. https://doi.org/10.1785/0120230307

Lee, E.-J., Chen, P., Jordan, T. H., Maechling, P. B., Denolle, M. A. M., & Beroza, G. C. (2014). Full-3-D tomography for crustal structure in Southern California based on the scattering-integral and the adjoint-wavefield methods. *Journal of Geophysical Research: Solid Earth*, *119*(8), 6421–6451. https://doi.org/10.1002/2014jb011346

Lomax, A. (2020). Absolute location of 2019 Ridgecrest seismicity reveals a shallow Mw 7.1 hypocenter, migrating and pulsing Mw 7.1 foreshocks, and duplex Mw 6.4 ruptures. *Bulletin of the Seismological Society of America*, *110*(4), 1845–1858. https://doi.org/10.1785/0120200006

Lomax, A., Michelini, A., Curtis, A., & Meyers, R. A. (2009). Earthquake location, direct, global-search methods. *Encyclopedia of Complexity and Systems Science*, *5*, 2449–2473. https://doi.org/10.1007/978-0-387-30440-3_150

Lomax, A., Virieux, J., Volant, P., & Berge-Thierry, C. (2000). Probabilistic earthquake location in 3D and layered models: Introduction of a Metropolis-Gibbs method and comparison with linear locations. *Advances in Seismic Event Location*, 101–134.

Lu, Y., & Ben-Zion, Y. (2022). Regional seismic velocity changes following the 2019 M w 7.1 Ridgecrest, California earthquake from autocorrelations and P/S converted waves. *Geophysical Journal International*, *228*(1), 620–630. https://doi.org/10.1093/gji/ggab350

Ma, S. (2010). Focal depth determination for moderate and small earthquakes by modeling regional depth phases sPg, sPmP, and sPn. *Bulletin of the Seismological Society of America*, *100*(3), 1073–1088. https://doi.org/10.1785/0120090103

Monastero, F. C., Katzenstein, A. M., Miller, J. S., Unruh, J. R., Adams, M. C., & Richards-Dinger, K. (2005). The Coso geothermal field: A nascent metamorphic core complex. *Geological Society of America Bulletin*, *117*(11–12), 1534–1553. https://doi.org/10.1130/b25600.1

Münchmeyer, J., Saul, J., & Tilmann, F. (2024). Learning the deep and the shallow: Deep-learning-based depth phase picking and earthquake depth estimation. *Seismological Research Letters*, *95*(3), 1543–1557. https://doi.org/10.1785/0220230187

Myers, S. C., Johannesson, G., & Hanley, W. (2007). A Bayesian hierarchical method for multiple-event seismic location. *Geophysical Journal International*, *171*(3), 1049–1063. https://doi.org/10.1111/j.1365-246x.2007.03555.x

Nazareth, J. J., & Hauksson, E. (2004). The seismogenic thickness of the southern California crust. *Bulletin of the Seismological Society of America*, *94*(3), 940–960. https://doi.org/10.1785/0120020129

Peterson, M., Vollmer, C., Brogan, R., Stracuzzi, D. J., & Young, C. J. (2021). Generating uncertainty distributions for seismic signal onset times. *Bulletin of the Seismological Society of America*, *111*(1), 11–20. https://doi.org/10.1785/0120200125

Qiu, Q., Barbot, S., Wang, T., & Wei, S. (2020). Slip complementarity and triggering between the foreshock, mainshock, and afterslip of the 2019 Ridgecrest rupture sequence. *Bulletin of the Seismological Society of America*, *110*(4), 1701–1715. https://doi.org/10.1785/0120200037

Rawlinson, N., Pozgay, S., & Fishwick, S. (2010). Seismic tomography: A window into deep Earth. *Physics of the Earth and Planetary Interiors*, *178*(3–4), 101–135. https://doi.org/10.1016/j.pepi.2009.10.002

Rawlinson, N., & Sambridge, M. (2005). The fast marching method: An effective tool for tomographic imaging and tracking multiple phases in complex layered media. *Exploration Geophysics*, *36*(4), 341–350. https://doi.org/10.1071/eg05341

Richards-Dinger, K. B., & Shearer, P. M. (2000). Earthquake locations in southern California obtained using source-specific station terms. *Journal of Geophysical Research*, *105*(B5), 10939–10960. https://doi.org/10.1029/2000jb900014

Ross, Z. E., Idini, B., Jia, Z., Stephenson, O. L., Zhong, M., Wang, X., et al. (2019). Hierarchical interlocked orthogonal faulting in the 2019 Ridgecrest earthquake sequence. *Science*, *366*(6463), 346–351. https://doi.org/10.1126/science.aaz0109

Roten, D., Olsen, K. B., & Day, S. M. (2017). Off-fault deformations and shallow slip deficit from dynamic rupture simulations with fault zone plasticity. *Geophysical Research Letters*, *44*(15), 7733–7742. https://doi.org/10.1002/2017gl074323

Ruan, Y., Lei, W., Modrak, R., Örsvuran, R., Bozdağ, E., & Tromp, J. (2019). Balancing unevenly distributed data in seismic tomography: A global adjoint tomography example. *Geophysical Journal International*, *219*(2), 1225–1236. https://doi.org/10.1093/gji/ggz356

Sambridge, M., & Mosegaard, K. (2002). Monte Carlo methods in geophysical inverse problems. *Reviews of Geophysics*, *40*(3), 3-1-3–29. https://doi.org/10.1029/2000rg000089

Samson, J. C., & Olson, J. V. (1980). Some comments on the descriptions of the polarization states of waves. *Geophysical Journal International*, *61*(1), 115–129. https://doi.org/10.1111/j.1365-246X.1980.tb04308.x

Sandwell, D. T., Zeng, Y., Shen, Z.-K., Crowell, B., Murray, J., McCaffrey, R., & Xu, X. (2016). The SCEC community geodetic model V1: Horizontal velocity grid. In *SCEC annu. Meeting*.

SCEDC. (2013). Southern California earthquake data center [Dataset]. *Caltech*. https://doi.org/10.7909/C3WD3xH1

Shaw, J. H., Plesch, A., Tape, C., Suess, M. P., Jordan, T. H., Ely, G., et al. (2015). Unified Structural representation of the southern California crust and upper mantle. *Earth and Planetary Science Letters*, *415*, 1–15. https://doi.org/10.1016/j.epsl.2015.01.016

Shinevar, W. J., Behn, M. D., Hirth, G., & Jagoutz, O. (2018). Inferring crustal viscosity from seismic velocity: Application to the lower crust of Southern California. *Earth and Planetary Science Letters*, *494*, 83–91. https://doi.org/10.1016/j.epsl.2018.04.055

Sibson, R. H. (1982). Fault zone models, heat flow, and the depth distribution of earthquakes in the continental crust of the United States. *Bulletin of the Seismological Society of America*, *72*(1), 151–163.

Sollberger, D., Bradley, N., Edme, P., & Robertsson, J. O. (2023). Efficient wave type fingerprinting and filtering by six-component polarization analysis. *Geophysical Journal International*, *234*(1), 25–39. https://doi.org/10.1093/gji/ggad071

Stein, S., & Wiens, D. A. (1986). Depth determination for shallow teleseismic earthquakes: Methods and results. *Reviews of Geophysics*, *24*(4), 806–832. https://doi.org/10.1029/rg024i004p00806

Tarantola, A. (2005). *Inverse problem theory and methods for model parameter estimation*. SIAM.

Taufiqurrahman, T., Gabriel, A.-A., Li, D., Ulrich, T., Li, B., Carena, S., et al. (2023). Dynamics, interactions and delays of the 2019 Ridgecrest rupture sequence. *Nature*, *618*(7964), 308–315. https://doi.org/10.1038/s41586-023-05985-x

Thompson Jobe, J. A., Philibosian, B., Chupik, C., Dawson, T., K. Bennett, S. E., Gold, R., et al. (2020). Evidence of previous faulting along the 2019 Ridgecrest, California, earthquake ruptures. *Bulletin of the Seismological Society of America*, *110*(4), 1427–1456. https://doi.org/10.1785/0120200041

Tian, D., Uieda, L., Leong, W. J., Fröhlich, Y., Grund, M., Schlitzer, W., et al. (2025). PyGMT: A Python interface for the Generic Mapping Tools (version v0.16.0). *Zenodo*. https://doi.org/10.5281/zenodo.15628725

Tong, P. (2024). Replication data for: Leveraging local depth phases for improved hypocenter analysis and discovery of a thick seismogenic zone in Ridgecrest, California (version V1) [Dataset]. *DR-NTU (Data)*. https://doi.org/10.21979/N9/BHCBP6

Tong, P., Li, T., Chen, J., & Nagaso, M. (2024). Adjoint-state differential arrival time tomography. *Geophysical Journal International*, *236*(1), 139–160. https://doi.org/10.1093/gji/ggad416

Tong, P., Yao, J., Liu, Q., Li, T., Wang, K., Liu, S., et al. (2021). Crustal rotation and fluids: Factors for the 2019 Ridgecrest earthquake sequence? *Geophysical Research Letters*, *48*(3), e2020GL090853. https://doi.org/10.1029/2020gl090853

Trugman, D. T., & Shearer, P. M. (2017). GrowClust: A hierarchical clustering algorithm for relative earthquake relocation, with application to the Spanish Springs and Sheldon, Nevada, earthquake sequences. *Seismological Research Letters*, *88*(2A), 379–391. https://doi.org/10.1785/0220160188

Tsai, Y.-B., & Aki, K. (1970). Precise focal depth determination from amplitude spectra of surface waves. *Journal of Geophysical Research*, *75*(29), 5729–5744. https://doi.org/10.1029/jb075i029p05729

Umino, N., Hasegawa, A., & Matsuzawa, T. (1995). sP depth phase at small epicentral distances and estimated subducting plate boundary. *Geophysical Journal International*, *120*(2), 356–366. https://doi.org/10.1111/j.1365-246x.1995.tb01824.x

University of Nevada, Reno. (1971). Nevada seismic network. *International Federation of Digital Seismograph Networks*. https://doi.org/10.7914/SN/NN

US Geological Survey, E. H. P. (2017). *Advanced National Seismic System (ANSS) comprehensive catalog of earthquake events and products: Various*. US Geological Survey.

Vidale, J. E. (1986). Complex polarization analysis of particle motion. *Bulletin of the Seismological Society of America*, *76*(5), 1393–1405.

Virtanen, P., Gommers, R., Oliphant, T. E., Haberland, M., Reddy, T., Cournapeau, D., et al. (2020). SciPy 1.0: Fundamental algorithms for scientific computing in Python. *Nature Methods*, *17*(3), 261–272. https://doi.org/10.1038/s41592-019-0686-2

Waldhauser, F., & Ellsworth, W. L. (2000). A double-difference earthquake location algorithm: Method and application to the northern Hayward fault, California. *Bulletin of the Seismological Society of America*, *90*(6), 1353–1368. https://doi.org/10.1785/0120000006

Wang, X., & Zhan, Z. (2020). Seismotectonics and fault geometries of the 2019 Ridgecrest sequence: Insight from aftershock moment tensor catalog using 3-D Green's functions. *Journal of Geophysical Research: Solid Earth*, *125*(5), e2020JB019577. https://doi.org/10.1029/2020jb019577

Weng, H., & Yang, H. (2017). Seismogenic width controls aspect ratios of earthquake ruptures. *Geophysical Research Letters*, *44*(6), 2725–2732. https://doi.org/10.1002/2016gl072168

Weston, J., Engdahl, E. R., Harris, J., Di Giacomo, D., & Storchak, D. A. (2018). ISC-EHB: Reconstruction of a robust earthquake data set. *Geophysical Journal International*, *214*(1), 474–484. https://doi.org/10.1093/gji/ggy155

White, M. C., Fang, H., Catchings, R. D., Goldman, M. R., Steidl, J. H., & Ben-Zion, Y. (2021). Detailed traveltime tomography and seismic catalogue around the 2019 M w7. 1 Ridgecrest, California, earthquake using dense rapid-response seismic data. *Geophysical Journal International*, *227*(1), 204–227. https://doi.org/10.1093/gji/ggab224

White, M. C., Fang, H., Nakata, N., & Ben-Zion, Y. (2020). PyKonal: A Python package for solving the eikonal equation in spherical and Cartesian coordinates using the fast marching method. *Seismological Research Letters*, *91*(4), 2378–2389. https://doi.org/10.1785/0220190318

Woodgold, C. R. (1999). Wide-aperture beamforming of depth phases by timescale contraction. *Bulletin of the Seismological Society of America*, *89*(1), 165–177. https://doi.org/10.1785/bssa0890010165

Yeck, W. L., Herrmann, B., Patton, J., Barnhart, W., & Benz, H. (2025). Estimating earthquake source depth using teleseismic broadband waveform modeling at the USGS National Earthquake Information Center. *Seismological Research Letters*, *96*(6), 3643–3655. https://doi.org/10.1785/0220240372

Yeh, T., & Olsen, K. B. (2023). Fault damage zone effects on ground motions during the 2019 M w 7.1 Ridgecrest, California, earthquake. *Bulletin of the Seismological Society of America*, *113*(4), 1724–1738. https://doi.org/10.1785/0120220249

Yu, C., Hauksson, E., Zhan, Z., Cochran, E. S., & Helmberger, D. V. (2019). Depth determination of the 2010 El Mayor-Cucapah earthquake sequence ($M \geq 4.0$). *Journal of Geophysical Research: Solid Earth*, *124*(7), 6801–6814. https://doi.org/10.1029/2018jb016982

Yu, Y., Ellsworth, W. L., & Beroza, G. C. (2025). Accuracy and precision of earthquake location programs: Insights from a synthetic controlled experiment. *Seismological Research Letters*, *96*(3), 1860–1874. https://doi.org/10.1785/0220240354

Yuan, J., Kao, H., & Yu, J. (2020). Depth-scanning algorithm: Accurate, automatic, and efficient determination of focal depths for local and regional earthquakes. *Journal of Geophysical Research: Solid Earth*, *125*(7), e2020JB019430. https://doi.org/10.1029/2020jb019430

Zhou, H. (1994). Rapid three-dimensional hypocentral determination using a master station method. *Journal of Geophysical Research*, *99*(B8), 15439–15455. https://doi.org/10.1029/94jb00934

Zhou, Z., Bianco, M., Gerstoft, P., & Olsen, K. (2022). High-resolution imaging of complex shallow fault zones along the July 2019 Ridgecrest ruptures. *Geophysical Research Letters*, *49*(1), e2021GL095024. https://doi.org/10.1029/2021gl095024

Zhu, L., & Helmberger, D. V. (1996). Advancement in source estimation techniques using broadband regional seismograms. *Bulletin of the Seismological Society of America*, *86*(5), 1634–1641. https://doi.org/10.1785/bssa0860051634

Zuza, A. V., & Cao, W. (2020). Seismogenic thickness of California: Implications for thermal structure and seismic hazard. *Tectonophysics*, *782*, 228426. https://doi.org/10.1016/j.tecto.2020.228426